

1 **Geophysical Trends inferred from 20 years of AIRS**
2 **infrared global observations**

3 **S. DeSouza-Machado¹, L. Larrabee Strow^{1,2}, R. Kramer³**

4 ¹JCET/GESTAR2, University of Maryland Baltimore County, Baltimore, Maryland

5 ²Dept of Physics, University of Maryland Baltimore County, Baltimore, Maryland

6 ³NOAA GFDL, Princeton New Jersey

7 **Key Points:**

- 8 • The 20+ year radiance record of NASA's AIRS sounder contains detailed verti-
9 cal information about changes in geophysical parameters.
10 • A novel method retrieves geophysical trends from the radiance record, using sta-
11 ble channels in radiance space and straightforward *a-priori*.
12 • Comparisons are made to trends from monthly Numerical Weather Prediction re-
13 analysis fields and L3 operational data products.

Corresponding author: Sergio DeSouza-Machado, sergio@umbc.edu

Abstract

Daily spectral radiance observations by NASA’s Atmospheric Infrared Sounder contain detailed information about surface and atmospheric temperature and water vapor. We obtain climate geophysical trends from 20 years (2002/09-2022/08) of AIRS observations using a novel method operating mostly in radiance space. The observations are binned into 3×5 degree tiles using 16 day intervals, after which nominally clear scenes are selected for each tile to construct the spectral radiance time series. De-seasonalized spectral trends are then obtained, which are inverted using a physical retrieval to obtain geophysical trends. This approach is distinct from traditional use of radiances whereby trends are generated after operational retrievals or assimilation into Numerical Weather Prediction models. Our approach rigorously ties the derived geophysical trends to the observed radiance trends, using far fewer computational resources and time. The retrieved trends are compared to trends derived from ERA5 and MERRA2 reanalysis model fields, and NASA Level3 AIRS v7 and CLIMCAPS v2 data. Our retrieved surface temperature trends agree quite well with ERA5, CLIMCAPS and the GISS surface climatology trends. Atmospheric temperature profile trends exhibit some variability amongst all these data sets, especially in the polar stratosphere. Water vapor profile trends are nominally similar among the data sets except for the AIRS v7 which exhibits drying trends in the mid troposphere. Spectral closure between observed trends and those computed by running the reanalysis and NASA L3 monthly fields through a radiative transfer code are discussed, with the major differences arising in the water vapor sounding region.

Plain Language Summary

The current generation of infrared sounders, designed for weather forecasting purposes, have been in orbit around the Earth for a long enough time to enable anomaly and trending studies for climate purposes. Traditionally their daily obtained radiance data has been used for operational atmospheric state retrievals, or assimilation into Numerical Weather Prediction models, after which climate anomaly studies are made. In this paper we use the raw radiance spectral data to form radiance anomalies and trends, after which we do a one step atmospheric state retrieval. This novel approach has the benefit of using only stable channels together with easily understood assumptions and well tested retrieval algorithms to do the trend or anomaly geophysical retrieval, which has full error characterization.

1 Introduction

NASA’s Atmospheric Infrared Sounder (AIRS) became operational in September 2002, as the first of the new generation of low noise, high stability hyperspectral sounders, making Top of Atmosphere (TOA) radiance observations at a typical 15km (at nadir) horizontal resolution. Follow on instruments with similar characteristics and abilities include the ESA’s Infrared Atmospheric Sounding Interferometer (IASI) and NOAA’s Cross Track Infrared Sounder (CrIS), operational since June 2007 and March 2012 respectively. The latter two already have follow on missions planned till the 2040s, and together these three sounders will provide scientists with a 40 year high quality, near continuous observational dataset for climate anomaly and trending studies.

Infrared radiances contain a wealth of information, including but not limited to surface temperature, atmospheric temperature and water amount, and mixing ratios of greenhouse gases such as carbon dioxide CO_2 , CH_4 and N_2O . Measurements by visible imagers which have ~ 1 km horizontal resolution or better King et al. (2013) suggest global cloud free fractions of $\sim 30\%$, but the 15 km footprint of typical sounders means at most 5% of the hyperspectral observations can be considered “cloud-free.” Current operational NASA L2 products use the method of cloud clearing on observed radiances in partly cloudy scene conditions before doing the geophysical retrieval. The cloud clearing method solves

64 for an estimate of clear column radiances by examining adjacent Fields of View (FOVs)
 65 to estimate the cloud effects on observed allsky radiances, assuming any differences are
 66 solely due to different cloud amounts in each FOV, and significantly increases geophys-
 67 ical retrieval yields (to about 50-60%) Smith and Barnet (2023). This does introduce in-
 68 creased noise in the cloud cleared radiances of the lower atmosphere sounding channels;
 69 in addition the subsequent retrieval depends on the first guess (which is a neural net for
 70 AIRS v7 and MERRA2 reanalysis for CLIMCAPS v2). The reader is referred to Susskind
 71 et al. (2003); Smith and Barnet (2020, 2023) for more details.

72 In this paper we work directly in radiance space and form either anomalies or trends
 73 from the underlying well characterized and understood radiances Strow and DeSouza-
 74 Machado (2020), in order to do a geophysical trend or anomaly retrieval. The work pre-
 75 sented here, once the averaged/sorted data is available, can be processed in hours to days,
 76 and can be duplicated by small research groups with ease. Moreover, our novel approach
 77 has zero temperature *a-priori* and minimal water vapor *a-priori*. This completely sidesteps
 78 time variability and the accuracy of the *a-priori* which causes errors in the retrievals,
 79 and ensures our work examines trends directly inferred from the radiances versus those
 80 from traditional methods. This leads to more unbiased results that directly highlight the
 81 conditions (for example stratospheric water vapor) where the sensor has limited sensi-
 82 tivity.

83 The approaches used in this work are therefore very different than climate anoma-
 84 lies or trends from reanalysis products or traditional Level 2 retrievals, neither of which
 85 are tailored for climate trends. Reanalysis products assimilate individual sensor scenes
 86 from many different instruments, and may have discontinuities as different instruments
 87 come online or go offline. Traditional Level 2 (and Level 3 products derived from Level
 88 2) retrieve the atmospheric state for individual scenes (or effective cloud-cleared radi-
 89 ance derived from a 3x3 grid of individual scenes). Both reanalysis and Level 2 prod-
 90 ucts require large computational resources, that preclude full dataset re-processing to
 91 help fully understand trends. A main characteristic of traditional L2 retrievals is the re-
 92 quirement for a good *a-priori* state for each inversion, making errors in the *a-priori* dif-
 93 ficult to distinguish from true variability in the data, especially with regard to trends.

94 The stability and accuracy of the AIRS instrument is documented in recent work
 95 on analyzing 16 years of AIRS radiance anomalies over cloud-free ocean Strow and DeSouza-
 96 Machado (2020). Geophysical retrievals on the anomalies yielded CO₂, CH₄, N₂O and
 97 surface temperature time series that compared well against in-situ data from NOAA Global
 98 Monitoring Laboratories (GML) trace gas measurements and NOAA Goddard Institute
 99 of Space Studies (GISS) surface temperature data respectively. A significant difference
 100 between this paper and Strow and DeSouza-Machado (2020) is the nominally clear scenes
 101 used in this paper are selected uniformly from all over the Earth, while the clear scenes
 102 in the latter were zonal averages which were sometimes concentrated in certain regions.

103 In this paper we expand upon our initial zonal clear sky analysis, to derive geophys-
 104 ical trends from 20 years (September 2002 - August 2022) of AIRS measurements over
 105 $\sim 3 \times 5$ degree tiles covering the Earth, chosen such that the number of observations
 106 in each tile is roughly equal. An important concept introduced is spectral closure, whereby
 107 the observed clear sky spectral radiance trends are compared to spectral trends produced
 108 by running the monthly reanalysis or official NASA retrieved AIRS L3 products through
 109 an accurate clear sky radiative transfer code; close agreement in different sounding re-
 110 gions (such as 640-800 cm⁻¹ for temperature and CO₂, 1350-1640 cm⁻¹ for water va-
 111 por, 1000-1150 cm⁻¹ for O₃) between the computed and actual observed spectral trends
 112 imply that trends from those geophysical parameters used in the computations are real-
 113 istic while disagreement suggests otherwise. A companion paper will utilize the geo-
 114 physical trend results to derive Outgoing Longwave Radiation (OLR) trends and non-
 115 local clearsky feedback parameters. Nominally clear scenes for each tile are picked out

116 using a quantile approach; from the time series, radiances trends are made over the en-
117 tire Earth, from which geophysical trends are retrieved.

118 Observed infrared spectral trends from AIRS has already been a focus of earlier
119 work by Huang et al. (2023) who studied a slightly shorter time period (2002-2020) while
120 Raghuraman et al. (2023) converted the radiances to Outgoing Longwave radiation (OLR),
121 but neither study involve retrievals from spectral trends to geophysical trends. Instead
122 they convert various model trends (such as ERA5) to spectral trends and compare against
123 the observed spectral trends. Our earlier work shows we can accurately account for the
124 effects of GHG forcings (Strow et al., 2021). In this paper we remove these GHG forc-
125 ings from the observed AIRS spectral trends to concentrate on atmospheric temperature
126 and water vapor and surface temperature, while the papers by Huang et al. (2023); Raghu-
127 raman et al. (2023) include the GHG forcings in the model generated spectral trends.
128 Another noteworthy examination of the time evolution of high spectral resolution infrared
129 radiances (converted to spectral outgoing longwave radiation (OLR) fluxes) by (Whitburn
130 et al., 2021) covered 10 years (2007-2017) of IASI observations. They confirmed that the
131 IASI-derived fluxes agreed well with increases in GHG gas concentrations and El-Nino
132 Southern Oscillation (ENSO) events within that time frame. A more recent paper Roemer
133 et al. (2023) used the 10 year IASI data to derive allsky longwave feedback spectral com-
134 ponents (water vapor, CO₂, window, ozone) and total values, while also estimating clear
135 sky feedback values.

136 We will refer to our results as the AIRS Radiance Trends (AIRS_RT). Compar-
137 isons are made against monthly output from the European Center for Medium Weather
138 Forecast fifth generation reanalysis (ERA5) Hersbach et al. (2020) and NASA’s second
139 generation Modern-Era Retrospective analysis for Research and Applications (MERRA2)
140 Gelaro and Coauthors (2017), and also against the official monthly AIRS L3 products
141 which are AIRS v7 L3 Susskind et al. (2014); Tian et al. (2020) and CLIMCAPS v2 L3
142 Smith and Barnett (2019, 2020). Detailed geophysical trends and spectral closure stud-
143 ies are presented for the averaged ascending (daytime (D)) and descending (nighttime (N))
144 trends; the appendix briefly discusses separate D and N trends.

145 2 Datasets used in this study

146 Three main types of datasets are used in this study. The first is the AIRS L1C ra-
147 diance dataset we analyzed for this paper, which has both daytime (D) and nighttime (N)
148 (ascending and descending) views of the planet. Second is the monthly operational L3
149 retrieval data, which are the AIRS v7 and the CLIMCAPS v2 products, also separated
150 into D/N data. Finally we also compared to trends from ERA5 and MERRA2 monthly
151 reanalysis model fields. The ERA5 monthly dataset is available in 8 averaged time steps,
152 so we match to the average AIRS overpass times and compute (D/N) data over the 20
153 years, while MERRA2 monthly model fields are only available as one time step; included
154 here for completeness we mention the NASA GISS surface temperature dataset, which
155 like MERRA2 is only available as a monthly mean. This means four of the datasets : AIRS_RT
156 (from AIRS L1C), AIRS L3 and CLIMCAPS L3, and ERA5 are separable into D/N, while
157 the other two (MERRA2 and GISS) are only available as a diurnal averaged value. We
158 describe these datasets in more detail below.

159 2.1 The AIRS instrument and L1C dataset

160 The Atmospheric Infrared Sounder (AIRS) on board NASA’s polar orbiting EOS/Aqua
161 platform has 2378 channels, covering the Thermal Infrared (TIR) spectral range (roughly
162 649-1613 cm⁻¹) and shortwave infrared (2181-2665 cm⁻¹). The full widths at half max-
163 imum satisfy $\nu/\delta\nu \sim 1200$. The (spectral dependent) noise is typically $\leq 0.2\text{K}$. The orig-
164 inal L1b radiance dataset suffers from spectral gaps and noise contaminated data as de-
165 tectors slowly fail. These limitations are addressed using a 2645 L1c channel dataset, where

166 spectral gaps and some of the noise “pops” are filled in using principal component recon-
 167 struction Manning et al. (2020) and is the dataset used to subset radiances analyzed in
 168 this paper. However we note that the results described in this paper used only the ac-
 169 tual observed radiances in pristine, stable channels described in Strow et al. (2021) and
 170 none of the synthetic channels. The Aqua platform is a polar orbiting satellite with 1.30
 171 am descending (night time over equator) and 1.30 pm ascending (daytime over equator)
 172 tracks. Each orbit takes about 90 minutes, with the 16 passes yielding almost twice daily
 173 coverage of the entire planet. About ~ 3 million AIRS spectral observations have been
 174 obtained daily since AIRS became operational in late August 2002. The instrument has
 175 provided data almost continuously since then though there have been some shutdowns
 176 (each spanning a few days) such as during solar flare events.

177 In this paper we use the re-calibrated 2645 channel L1C radiance data Strow and
 178 DeSouza-Machado (2020) instead of the 2378 L1B data. 20 years (spanning September
 179 1, 2002-August 31, 2022) of AIRS L1C radiance data is gridded into 4608 tiles covering
 180 the Earth : 72 longitude boxes which are all 5° in width, and 64 latitude boxes which are
 181 approximately 2.5° in width at the tropics but wider at the poles to keep the number of
 182 observations per 16 day intervals (which is the repeat cycle of the AIRS orbit on the Aqua
 183 satellite) roughly the same. This way there are ~ 12000 observations per 16 days per tile,
 184 which are roughly equally divided between the ascending/daytime (D) and descending/nighttime
 185 (N) tracks. In this paper we discuss results for both the ascending and descending tracks
 186 using a retrieval based on the longwave (LW) and midwave (MW) regions of the spec-
 187 trum ($640\text{-}1620\text{ cm}^{-1}$ or $6\text{-}15\ \mu\text{m}$).

188 In this paper our trend retrievals use only the AIRS channels are stable in time,
 189 as quantified in Strow et al. (2021). For example the shortwave (SW) channels are drift-
 190 ing at a higher rate than the LW/MW channels, which can lead to incorrect surface tem-
 191 perature rates, and are avoided in this paper. Similarly there are many channels in
 192 the LW and MW whose detectors are drifting in time, and which are also not used here.
 193 For example there are some higher wavenumber (shorter wavelength) channels past the
 194 ozone band which have a significant drift in time, possibly due to changes in the polar-
 195 ization of the scan mirror coating with time. Therefore compared to other AIRS oper-
 196 ational products used in this paper, our results use channels that are demonstrated to
 197 have high stability Strow et al. (2021). We do note that some of the observed drifts in
 198 the AIRS channels stabilized after 6 years, so their impact is reduced when looking at
 199 20 year trends.

200 **2.2 Reanalysis Model fields**

201 The ERA5 fifth generation reanalysis product from the European Center for Medium
 202 Range Weather Forecasts is freely available on monthly timescales from the Copernicus
 203 Climate Data Store. This monthly dataset is output at 37 pressure levels at 0.25° horizontal
 204 resolution Hersbach et al. (2020), which is further subdivided into eight 3-hour averages
 205 per month (corresponding to 00,03,06,...21 UTC). For each month from September 2002-
 206 August 2022 we downloaded the surface temperature and pressure fields, as well as at-
 207 mospheric temperature, water vapor and ozone fields. These are then colocated to each
 208 tile center using 2D spatial interpolation, as well as time interpolated according to the
 209 average AIRS overpass time as a function of month. From the resulting monthly time-
 210 series of reanalysis model fields for each tile, we generated (a) thermodynamic trends for
 211 surface temperature, air temperature, water vapor and ozone model fields (b) a 20 year
 212 average thermodynamic profile in order to produce jacobians for the linear trend retrievals
 213 (c) by using the model fields as input to the clear sky SARTA radiative transfer code Strow,
 214 Hannon, DeSouza-Machado, et al. (2003) a monthly time series of clear sky radiances
 215 for each tile was generated, from which we could compute radiance trends. We did this
 216 for both the ascending and descending datasets.

217 The MERRA version 2 (MERRA2) re-analysis used in this paper is the second gen-
 218 eration Gelaro and Coauthors (2017) product from NASA’s Global Modeling and As-
 219 similation Office. The monthly data we use is available on 42 pressure levels at a hor-
 220 izontal resolution of $0.5^\circ \times 0.625^\circ$, but only one monthly mean diurnally averaged out-
 221 put is available per month. Similar to the ERA5 output, we colocated the MERRA2 sur-
 222 face temperature, atmospheric temperature, water vapor and ozone fields to our tile cen-
 223 ters for each month starting September 2002 in order to produce a time series of radi-
 224 ance and model output, from which radiance and thermodynamic trends could be com-
 225 puted for comparisons against other datasets in this study; similar to above we also gen-
 226 erated a monthly time series of clear sky radiances for each tile, from which we could com-
 227 pute clear sky radiance trends based on MERRA2.

228 The NASA Goddard Institute of Space Studies (GISS) surface temperature data
 229 v4 surface temperature data 2023 (2005); Lenssen et al. (2019) is a monthly dataset based
 230 primarily on near surface temperatures land stations, and data from ships and buoys.
 231 As with MERRA2 we obtained one monthly mean dataset per month, which we could
 232 not separate into descending (N) or ascending (D) tracks.

233 2.3 AIRS L3 Products

234 NASA routinely produces two retrievals from the AIRS L1C data observed each
 235 day, which are AIRS v7 Susskind et al. (2014); Tian et al. (2020) and CLIMCAPS v2
 236 Smith and Barnett (2019, 2020). Both use the cloud clearing process but there are sig-
 237 nificant algorithmic differences; in particular the AIRS v7 product is initialized by a neu-
 238 ral net, while CLIMCAPS uses MERRA2 for its initialization. The L2 products are then
 239 individually turned into L3 monthly products, for both the ascending (daytime) and de-
 240 scending (nighttime) data. The timeseries of thermodynamic profiles were used as in-
 241 put to the clear sky SARTA RTA to generate radiances, after which radiance trends and
 242 thermodynamic trends are also produced.

243 2.4 Other L3 Products

244 The Microwave Limb Sounder (MLS) monthly binned water vapor (H₂O) mixing
 245 ratio dataset Lambert et al. (2021), which contains data at spatial coverage $\pm 82^\circ$ lat-
 246 itude, at a spatial resolution of $4^\circ \times 5^\circ$ and useful vertical range between 316 and 0.00215
 247 hPa was used in this paper to improve retrieval trends in the upper atmosphere.

248 3 Filtering the Observational Data for clear scenes

249 Here we discuss the “clear scene” selection from all the observed data stored for each
 250 of the 72×64 tiles. Ideally we would prefer to use a MODIS cloud fraction product (1
 251 km) colocated to the 15 km AIRS footprints, but this is presently unavailable. Our ear-
 252 lier work used an uniform clear flag over ocean Strow et al. (2021) which will not work
 253 well over land because of surface inhomogeneity. In this section we discuss an alterna-
 254 tive clear filter based on the hottest 10 percent of AIRS observations that are present
 255 inside any 16 day tile, over any location.

256 3.1 Observed BT1231 Distributions

257 The radiances measured in thermal infrared window region ($800\text{-}1000\text{ cm}^{-1}$ and
 258 $1100\text{-}1250\text{ cm}^{-1}$) are dominated by the effects of the surface temperature, water vapor
 259 continuum absorption and cloud/aerosol effects. The effects of water vapor continuum
 260 absorption is largest in hot and humid tropical scenes (depressing the observations rela-
 261 tive to surface temperatures by about 5-6 K, which reduces to about 2 K at $\pm 50^\circ$) and
 262 is almost negligible for cold, dry scenes (less than 1 K). Scattering and absorption by liq-

263 uid and ice clouds also affects the window region (Deep Convective Clouds can depress
 264 the window channel observations by as much as 100 K relative to surface temperatures).
 265 For each tile, we use the 1231.3 cm⁻¹ observation as our representative window chan-
 266 nel (AIRS LIC channel ID = 1520), as it is minimally impacted by weak water vapor
 267 lines. Changed to Brightness temperature (BT) the observation in this 1231.3 cm⁻¹ chan-
 268 nel (BT1231) therefore serves as a measure for the cloudiness of an observation : if there
 269 are no or low or optically thin clouds, it will effectively measure the surface temperature,
 270 but as the clouds get thicker and higher, it will measure the cold cloud top temperatures.
 271 For any tile during any 16 day observation periods, we can compute quantiles \mathcal{Q} based
 272 on the observed BT1231 to screen between cloudy and partially clear scenes. We chose
 273 different BT1231 quantiles (so quantile $\mathcal{Q}0.XY$ will have a numerical value $BT1231_{\mathcal{Q}0.XY}$
 274 associated with it) and show below the data contained between $\mathcal{Q}0.90$ and $\mathcal{Q}1.00$ can
 275 be considered “almost free of clouds.”

276 Figure 1 shows all the BT1231 observations for a chosen 16 day timestep in the form
 277 of a zonally averaged histogram (normalized probability distribution functions (PDFs)),
 278 with latitude on the vertical axis and BT1231 on the horizontal axis. The colorbar is the
 279 PDF value, and we used data spanning August 27, 2012 - September 11, 2012 which is
 280 approximately half way through the 20 year AIRS mission dataset used in this paper.
 281 The curves show the zonally averaged BT1231 values of the minimum ($\mathcal{Q}0.00$) in dark
 282 cyan, mean (thick red), median ($\mathcal{Q}0.50$ in orange), maximum ($\mathcal{Q}1.00$ in light cyan); also
 283 shown are a handful of other zonally averaged BT1231 values, for example $\mathcal{Q}0.80$, $\mathcal{Q}0.90$
 284 (thick black curve), $\mathcal{Q}0.95$ and $\mathcal{Q}0.97$. The distributions are skewed to the left (nega-
 285 tive skewness), as confirmed by the mean being less than the median. We also point out
 286 that even $\mathcal{Q}0.80$ sees much of the surface from the southern tropics to the northern pol-
 287 ar region. The 220 K horizontal axis cutoff means we do not see the very cold (190 K)
 288 observations over the winter Antarctic.

289 The figure shows the expected qualitative features, for example (1) the tropical PDFs
 290 peak at around 295 K, but show some warmer observations, as well much colder obser-
 291 vations (below 230 K) corresponding to Deep Convective Clouds (DCC); this gives a dy-
 292 namic range of almost 100 K at the tropics (2) the BT1231 observed over the Southern
 293 Polar (polar winter) regions are much colder than the BT1231 observed over the North-
 294 ern Polar (polar summer) regions and (3) the reddish peaks in the 30°N - 40°N are a com-
 295 bination of the marine boundary layer (MBL) clouds and warmer summer land temper-
 296 atures. Figure 1 shows on average the cloud effect at the tropics is an additional mod-
 297 est 20 K (difference between $\mathcal{Q}0.90$ and $\mathcal{Q}0.50$) compared to the 100 K dynamic range.
 298 This is because the cloud fractions and cloud decks in the individual observations have
 299 effectively more clouds (with larger cloud fraction in the FOV) lower in the atmosphere
 300 than higher up; the net effect is that in the window region the atmosphere is on aver-
 301 age radiating from the lower (warmer) altitudes, and so spectra whose BT1231 values
 302 are larger than $BT1231_{\mathcal{Q}0.80}$, see much of the surface emission as well.

303

304 We now use the above plots to select “almost clear” scenes. For any one tile, we de-
 305 fine set $\Psi_{0.XY}$ to have all observations i whose BT1231 lies between quantiles $\mathcal{Q}0.XY$
 306 and $\mathcal{Q}1.00$, $\{i \mid BT1231_{\mathcal{Q}0.XY} \leq BT1231(i) \leq BT1231_{\mathcal{Q}1.00}\}$. In what follows $\mathcal{Q}0.XY$
 307 is the radiances averaged over all the observations i which are in the set $\Psi_{0.XY}$, namely

$$r_{\mathcal{Q}0.XY}(\nu) = \frac{1}{N_{0.XY}} \sum_{i \in \Psi_{0.XY}} r_i(\nu) \quad (1)$$

308 where $r_i(\nu)$ are the $N_{0.XY}$ individual observations in set $\Psi_{0.XY}$. In this section we only
 309 use the $\nu = 1231$ cm⁻¹ channel, but in later sections we easily form averages for all 2645
 310 channels, at any 16 day time step for any tile.

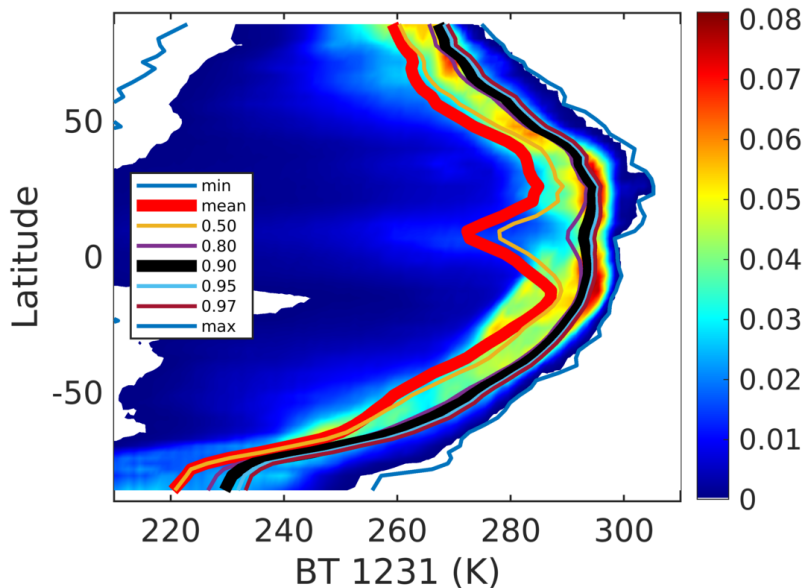


Figure 1. Zonally averaged BT1231 normalized histograms (probability distribution functions) as a function of latitude and temperature bin, for an 2012/08/27 - 2012/09/11 timespan (colorbar) and quantiles (curves). The thick black curve is the $Q_{0.90}$ quantile (and above) used in this paper, and is very close to the maximum $Q_{1.00}$ quantile.

311 We tested different quantile sets $\Psi_{0.XY}$ to see which one can reliably be considered
 312 to provide a nominally “cloud free” global dataset, and chose the $Q_{0.90}$ average (ie de-
 313 fined as averaged over the $\Psi_{0.90}$ set) as the one to use for the rest of this paper, unless
 314 explicitly stated otherwise. The tests primarily involved comparisons to scenes produced
 315 by the uniform/clear sky filter described in Strow and DeSouza-Machado (2020) for the
 316 same August 27, 2012 - September 11, 2012 sixteen day timespan. This latter filter se-
 317 lects clear scenes by both testing for uniformity (to within 0.5 K) across a 3×3 group-
 318 ing of AIRS scenes and also using a criteria that the observed window channel observa-
 319 tions should be within ± 4 K of clear-sky simulations using thermodynamic parameters
 320 supplied by reanalysis models. The results are shown in the left hand plot of Figure 2,
 321 plotted on a $1^\circ \times 1^\circ$ grid. We note in this plot the uniform/clear scenes that are plotted
 322 are limited to those over ocean, and for solar zenith less than 90° (daytime), which au-
 323 tomatically filtered out many of the views over the (wintertime) Southern Polar region.
 324 Immediately apparent are the gaps produced by the uniform/clear filter *e.g.* in the Trop-
 325 ical West Pacific or off the western coasts of continents where there are clouds. The gaps
 326 can be changed by *e.g.* changing the 4K threshold to allow more or fewer scenes through
 327 the filter.

328 The center plot shows for all tiles, the daytime scenes selected by the $Q_{0.90}$ filter
 329 for the same time period, on the same $1^\circ \times 1^\circ$ grid. Compared to the left hand plot, the
 330 spatial coverage is almost complete, as the $Q_{0.90}$ average always has the hottest 10% of
 331 the observations. At this 1° resolution, used for comparison with the uniform/clear grid
 332 filter described in the previous paragraph, gaps are seen in regions where for example
 333 the local topography means observations over mountains would be colder than the sur-
 334 rounding coastal or plain regions. This is not a concern since zooming back out to the
 335 coarser $3^\circ \times 5^\circ$ tile resolution, will include $Q_{0.90}$ data for the quantile and trending anal-
 336 ysis.

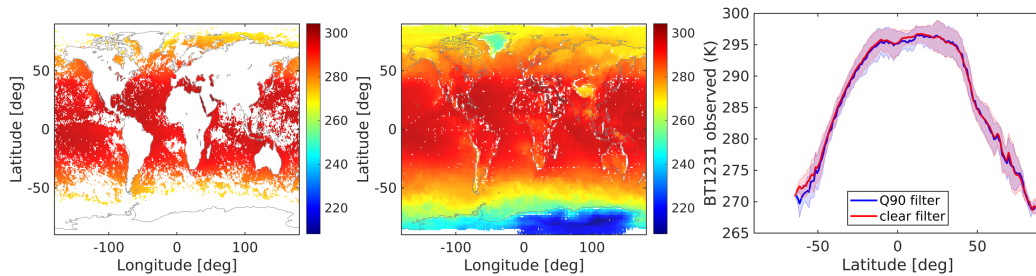


Figure 2. Clear scenes for the same 2012/08/27 - 2012/09/11 timespan selected by (left) an uniform/clear sky filter and (center) the Q0.90 average described in this paper. The right hand plot shows the mean (over ocean) observed BT1231 as a function of latitude, for the two selections; the difference is about $0 \text{ K} \pm 1 \text{ K}$ in most region except in the southern midlatitudes where the Q0.90 average produced scenes that were about 1 K cooler on average.

337 To compare the mean observations we remove the over-land and over-polar region
 338 data from the center plot. The right hand plot shows the mean observed BT1231 from
 339 the $1^\circ \times 1^\circ$ grid from the uniform/clear sky filter as a function of latitude, compared to
 340 the $1^\circ \times 1^\circ$ grid from the Q0.90 scenes. The difference between the uniform/clear versus
 341 Q0.90 average is within about $0.25 \text{ K} \pm 1 \text{ K}$ across the southern tropics to the north-
 342 ern midlatitudes, though the bias rises to about 1 K by about -50°S . We consider this
 343 an acceptable difference, as we could tune the thresholds for the uniform/clear filter to
 344 *e.g.* change the areal coverage and/or number of clear scenes and hence comparisons to
 345 the Q0.90 scenes.

346

347 The results presented in this section have been checked for robustness, using other
 348 16 day intervals spanning the four seasons. We conclude that for any 16 day timestep
 349 the radiances used in the Q0.90 average (a) produces almost complete spatial coverage
 350 of the Earth, (b) selects scenes whose average BT1231 is very close to the average BT1231
 351 from scenes selected using an uniform/clear filter (c) trends from that quantile typically
 352 differ by less than $\pm 0.002 \text{ K yr}^{-1}$ from the other quantiles and (d) this selection pro-
 353 duces spectral trends which compare well against those obtained from the quality assured
 354 binned AIRS CCR data record Manning (2022). Together these imply the Q0.90 aver-
 355 age is an acceptable proxy for “clear scenes”. For the remainder of the paper we there-
 356 fore consider Q0.90 as consisting of nominally clear observations whose BT1231 lies be-
 357 tween the 90th quantile and hottest observation. Our retrievals using this $\mathcal{Q}0.90 \rightarrow \mathcal{Q}1.00$
 358 averaged dataset (shortened to Q0.90) is referred to as AIRS_RT in what follows.

359

3.2 Observed trends from the Q0.90 Quantiles

360

361 Having selected the Q0.90 observations, for each tile the average radiance per 16
 362 day interval is computed. With two sixteen day periods not available (*Aqua* platform
 363 or AIRS shutdowns during *e.g.* solar flare events) this gives a total of 457 time steps over
 364 20 years. Anomalies are formed from this time series, and then de-seasonalized to give
 365 the spectral radiance trends and error estimates Strow and DeSouza-Machado (2020) us-
 ing Matlab *robustfit*:

$$r_{\text{observations}}^{16 \text{ days}}(t) \sim r_{\text{fit}}(t) = r_o + a_1 t + \sum_{i=1}^4 c_i \sin(n2\pi t + \phi_i) \quad (2)$$

with a_1 and its associated uncertainty, both converted to brightness temperature (BT), being the trends in K yr^{-1} . Using sub-harmonics in the fit did not produce any noticeable change in the AIRS_RT retrievals (described below).

The left panel of Figure 3 shows the descending orbit (nighttime) 20 year (September 2002- August 2022) global averaged spectral observations for the five quantiles mentioned above. We note the spectra in most of the plots in this section are weighted by the $\cosine(\text{latitude})$ of the tiles, unless otherwise stated. In addition we only show the $640\text{-}1640\text{ cm}^{-1}$ region, and ignore the shortwave $2050\text{-}2750\text{ cm}^{-1}$ region since the AIRS SW channels are drifting relative to the LW Strow and DeSouza-Machado (2020). Spectral averages constructed from Figure 1 would have this same behavior, namely that in the window region the mean spectrum of data populating the warmer quantiles (Q0.80, Q0.90, Q0.95, Q0.97) as defined in Equation 1 are on the order of a Kelvin apart, and have about half/quarter that difference in the optically thicker regions dominated by H_2O and/or CO_2 absorption respectively.

The right hand panel of Figure 3 shows (top) the trends and (bottom) the 2σ trend uncertainties for these quantiles, in K yr^{-1} . We emphasize that the top right panel shows that the spectral trends for the quantiles lie almost on top of each other; the difference between the Q0.50 and other trends is at most about $+0.003\text{ K yr}^{-1}$ (out of a 0.02 K yr^{-1} signal) in the window region (and about $+0.0045\text{ K yr}^{-1}$ in the troposphere temperature sounding channels), or less than 10%. Similarly the largest trend uncertainty in the bottom panel is for Q0.50. This implies that clouds effects in the infrared do produce the largest variability (blue curve) but on average for the infrared are not changing much, so the $+0.022\text{ K yr}^{-1}$ window region trends are dominated by surface temperatures changes and to a lesser extent by water vapor changes.

TOA radiances in the $15\text{ }\mu\text{m}$ ($700\text{-}800\text{ cm}^{-1}$) region are impacted by two effects (a) the increased optical depths due to increasing atmospheric CO_2 leads to atmospheric emission from higher altitudes/lower temperatures, resulting in almost a -0.06 K/year signal for the troposphere, and (b) the atmospheric temperature increases (again about $+0.02\text{ K yr}^{-1}$). Also of interest is the trends in the stratosphere ($650\text{-}700\text{ cm}^{-1}$) changes which consists of a stratospheric cooling signal (negative) and emission higher up due to increased CO_2 ; combining to give a net zero effect over 20 years, also seen in Raghuraman et al. (2023). The H_2O signal is evident in the $1400\text{-}1625\text{ cm}^{-1}$ region, and is only slightly positive; in other words, increasing temperatures have led to increased atmospheric amounts of H_2O , and the water vapor feedback has reduced the amount of outgoing flux in that region. By extension, this can only be expected to have happened in Far Infrared ($10\text{-}650\text{ cm}^{-1}$) spectral regions affected by water vapor, and cannot be wholly confirmed as current sounders do not make direct measurements in that region. In the near future it is anticipated the Far Infrared Outgoing Radiation Understanding and Monitoring (FORUM) mission Palchetti et al. (2020) will provide data to fill in this important observation gap.

4 Spectral closure : comparisons between observed and simulated spectral trends

Previous work Strow and DeSouza-Machado (2020) has demonstrated that the radiances from AIRS are climate quality, if one restricts the channel set to the ~ 450 channel set that is largely immune to nonphysical drifts Strow et al. (2021). In this section we describe a way to test the quality of the monthly thermodynamic output from reanalysis and/or L3 products which are all in geophysical space, against the AIRS L1C observational data which is in radiance space. This is accomplished by geolocating the monthly (ERA5) surface temperature, air temperature, water vapor and ozone fields to tile cen-

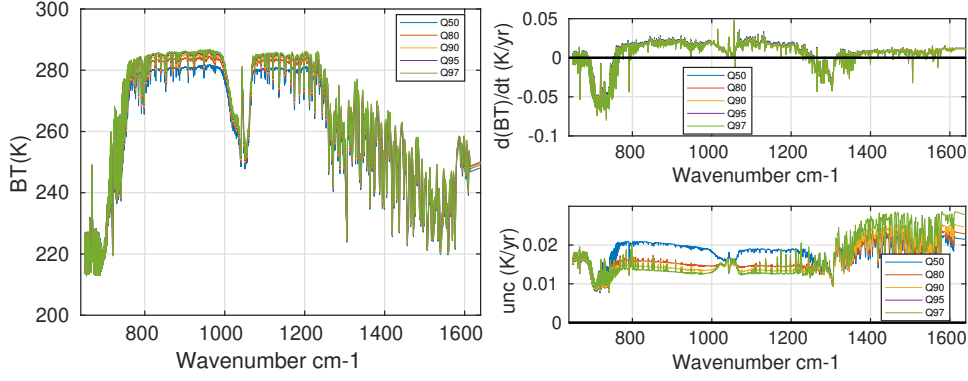


Figure 3. 20 year trends from different observation quantiles. The left hand panel shows the mean globally averaged BT observations from 20 years of AIRS data, for quantiles Q0.50,0.80,0.90,0.95,0.97 as described in the text. The right hand panel shows (top) the globally averaged trends for those different quantiles and (bottom) the spectral uncertainty in the trends. The nighttime (descending) trends are shown in these plots.

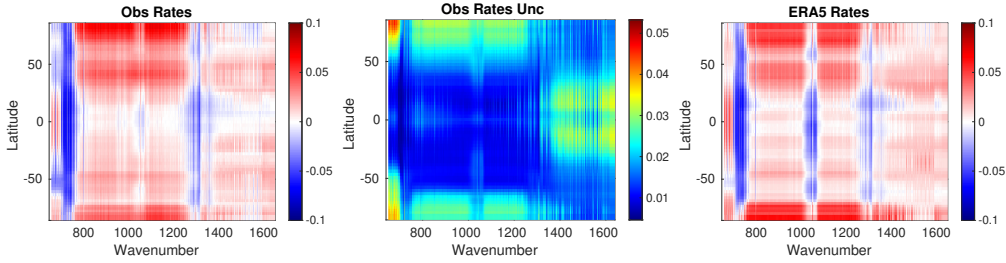


Figure 4. 20 year zonally averaged spectral brightness temperature trends (in K yr^{-1}) for (left) AIRS Q0.90 observations and (right) clear sky simulations using ERA5 monthly model fields. The center panel shows the AIRS Q0.90 spectral uncertainties. The ERA5 simulations included linear trends of CO_2 , CH_4 and N_2O , while the O_3 trends in ERA5 are from the reanalysis itself.

416 ters as described in Section 2.2, which are then input and run through the SARTA fast
 417 model Strow, Hannon, DeSouza-Machado, et al. (2003), for the entire 20 years. Spectral
 418 radiance trends were then computed from these time series of (clear sky) spectral
 419 radiances. The conversion of L3 retrieval and NWP reanalysis trends to a radiance time
 420 series, provides a rigorous check of their accuracy against the observed AIRS L1C ra-
 421 diance trends which are validated to be highly accurate.

422 The simulations included realistic column linearly-increasing-with time mixing ra-
 423 tios for CO_2 , CH_4 and N_2O for the ERA5 spectra, as well as land or ocean surface emis-
 424 sivity co-located to tile centers together with view angles of about 22° , which is the av-
 425 erage view angle of the tiled observations. From these the ERA5 spectral trends were
 426 derived similarly to what was described above for the AIRS observation spectral trends.

427

428 Figure 4 shows the AIRS observed Q0.90 (nominally clear) descending (night) zonally
 429 averaged results in K yr^{-1} in the left panel, and the zonally averaged simulated clearsky
 430 (without clouds) spectral trends (also in K yr^{-1}) from monthly ERA5 fields in the right

431 panel. The center panel shows the spectral trend uncertainties from the observations,
 432 also in K yr^{-1} . In the next section we derive geophysical trends from these (AIRS ob-
 433 served) spectral trends, and the similarities/ differences in geophysical trends between
 434 observations and models/operational data can be partially understood from the simi-
 435 larities/differences in the spectral trends. For example, the H_2O sounding region (1350 -
 436 1600 cm^{-1}) of the left and right panels of Figure 4 shows roughly similar (positive) spec-
 437 tral trends in the tropics and mid-latitudes; there are some slight differences in the high
 438 altitude channels (1450 - 1550 cm^{-1} region). The following sections shows that this re-
 439 sults in subtle differences in the tropospheric water vapor trends. Observations and sim-
 440 ulations both have positive dBT/dt in the 800 - 960 , 1150 - 1250 cm^{-1} region, indicating
 441 surface warming; however the ERA5 simulation show more warming in the southern pol-
 442 ar regions than do the AIRS observations. Note the mean warming in the tropics for
 443 both observations and ERA5 simulations is less than that in the mid-latitudes, and the
 444 polar regions show the largest overall change in brightness temperature in the window
 445 region. Large differences are seen in the 10 um (1000 cm^{-1}) O_3 sounding region, which
 446 are not surprising since ozone assimilation is not a primary goal of ECMWF assimi-
 447 lation; here we do not address these as we focus on the changes to the moist thermody-
 448 namic state. The window region trends computed using the ERA5 model are more posi-
 449 tive in the Southern Polar region. Conversely the 640 - 700 cm^{-1} spectral region is posi-
 450 tive, especially in the tropics; however the observations show a net cooling trend away
 451 from the tropics, compared to the ERA simulations. This demonstrates the importance
 452 of the model \rightarrow spectral trend comparisons, given the accuracy of the AIRS observations.

453 The paper by (Raghuraman et al., 2023) shows similar figures, but in terms of spec-
 454 tral OLR trends encompassing the 0 - 2000 cm^{-1} range, while (Huang et al., 2023) shows
 455 similar plots for a slightly smaller time period (2002-2020) using the nadir L1B radiance
 456 dataset which has no or minimal frequency corrections compared to the L1C set we use
 457 in this paper. (Huang et al., 2023; Raghuraman et al., 2023) and our work all show, ei-
 458 ther in radiance or OLR space, (a) the increased observed radiance in the window chan-
 459 nels, due to surface temperature increases (b) the $\simeq -0.06 \text{ K yr}^{-1}$ decrease in BT in the
 460 700 - 750 cm^{-1} troposphere sounding region, which is due to the CO_2 amounts increas-
 461 ing; we also see differences in the signs of the BT changes in the 650 - 700 cm^{-1} strato-
 462 spheric CO_2 and temperature channels for some latitudes between AIRS_RT observa-
 463 tions and ERA5 simulations (c) increases in the 1350 - 1640 cm^{-1} water vapor sounding
 464 region seen in Figures 3 and 5, and (d) the 1280 - 1340 cm^{-1} decreases are due to CH_4
 465 increases.

466 4.1 Sample spectral closure comparisons using other monthly products

467 Here we follow the earlier work of Huang et al. (2023) and convert the ERA5 monthly
 468 model fields to spectral radiances, after which we compute spectral trends for compar-
 469 ison to AIRS observations. Spectral closure calculations for the entire 20 year timeseries
 470 were also generated for the monthly MERRA2 model fields, as well as the monthly AIRS
 471 v7 L3 and CLIMCAPS L3 retrieved data products. Again only the monthly thermody-
 472 namics and surface temperature fields for all 72×64 tiles were used in these SARTA runs,
 473 with GHG changes added in for each timestep as described above. Spectral trends were
 474 then computed using Equation 2.

475 We chose just one limited example here to illustrate the power of this approach for
 476 diagnosing which dataset is more accurate, given that the AIRS spectral trend accuracy
 477 is already established. Water vapor is highly variable in space and time, meaning wa-
 478 ter vapor retrievals using hyperspectral sounders radiances differ most from NWP fore-
 479 casts, in particular because of the typical ± 90 minute difference between observation
 480 and forecast, and is where these sounders typically provide the most information. Fig-
 481 ure 5 show the globally averaged brightness temperature trends (in K yr^{-1}) in the 1350
 482 - 1650 cm^{-1} water vapor sounding region. The blue curve shows the trends from the AIRS

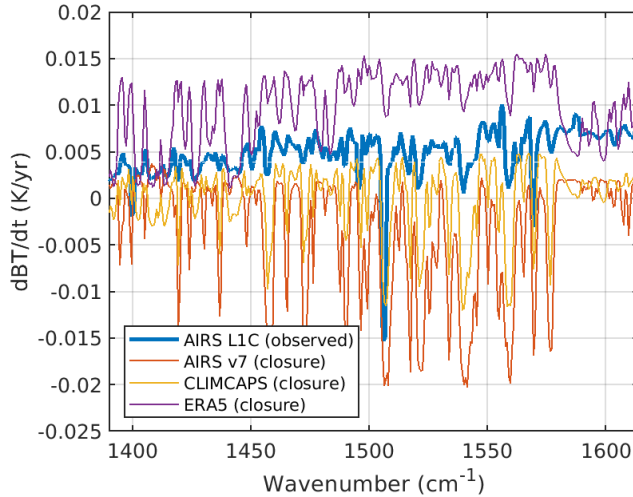


Figure 5. Globally averaged spectral trends in the water vapor sounding region : AIRS L1C observations (blue) compared to spectral closure from the standard monthly AIRS L3 retrievals (red) and CLIMCAPS L3 (yellow) and from monthly ERA5 simulations (purple). The reconstructed AIRS_RT trends very closely match the AIRS L1C observations and are not shown here.

483 observations used in this paper, while spectral trends constructed from the AIRS L3/
 484 CLIMCAPS L3 retrievals are in red/yellow and the ERA5 model fields are in purple. The
 485 AIRS observations and ERA5 constructed spectral trends are positive in this region, while
 486 the AIRS L3 and CLIMCAPS L3 trends are obviously different, being negative in this
 487 water vapor sounding region. The subtle differences in these spectral trends arise from
 488 differences in the geophysical trends between observations and the models themselves,
 489 and will be addressed in the following sections, where the retrieved and model surface
 490 temperature, and atmospheric temperature and water vapor geophysical trends will be
 491 compared and discussed.

492

493 **5 Testing the variability of representative points from NWP reanal-** 494 **ysis**

495 Each sixteen day $3^\circ \times 5^\circ$ tile contains ~ 12000 observations, which means for each
 496 tile about 600 daytime and 600 nighttime observations are averaged to produce the Q0.90
 497 dataset per timestep. Conversely there are typically only ~ 240 monthly ERA5 0.25° points
 498 per $3^\circ \times 5^\circ$ tile; for 1° resolution AIRS L3 and CLIMCAPS L3 there are even fewer (15)
 499 points per tile. This low number of points means we chose a simple solution of using the
 500 grid cell closest to the center of each $3^\circ \times 5^\circ$ tile for building the NWP and L3 geophys-
 501 ical time series. This choice is validated below using the following test to see for exam-
 502 ple how surface temperature trends would be impacted as we changed the representa-
 503 tive point for the ERA5 model fields.

504 For the descending overpass we built complete sets of approximately 240 ERA5 points
 505 per tile per month; at 0.25° resolution one of these is almost certainly at the tile center.
 506 From these monthly sets, we could either directly read the tile center temperature (our
 507 default), or compute the average surface temperature per tile, or compute the average
 508 of the hottest 10% surface temperatures per tile. This was done for all 20 years (240 monthly

509 timesteps) after which the three timeseries were trended. Over ocean the differences be-
 510 tween all three datasets was typically $-0.001 \pm 0.005 \text{ K yr}^{-1}$, while over land the differ-
 511 ences were about $0.001 \pm 0.01 \text{ K yr}^{-1}$. This is to be compared to mean trends of about
 512 $0.014 \pm 0.02 \text{ K yr}^{-1}$ over ocean and $0.025 \pm 0.04 \text{ K yr}^{-1}$ over land : the spread of the
 513 ocean and land ERA5 surface temperature trends for the three methods, is much smaller
 514 than the mean trends. Given that there were far fewer re-analysis points in a grid box
 515 than tiled Q0.90 observations, coupled with the fact that choosing the 10% warmest pro-
 516 files would provide an even smaller sample, we chose to use the tile center to be the rep-
 517 resentative point to co-locate the model fields.

518 6 Geophysical Trend Retrieval outline

519 6.1 Setting up the Retrieval Problem

520 The observed clear sky spectral brightness temperature for a tile at any time t can
 521 be modeled as

$$BT(\nu, t) = f(X(t), \epsilon(\nu, t), \theta(t)) + NeDT(\nu) \quad (3)$$

522 where the state vector $X(t)$ has the following five geophysical state parameters : (1) sur-
 523 face temperature (ST), (2) atmospheric temperature profile $T(z)$, (3) water vapor pro-
 524 file $WV(z)$, (4) ozone profile $O3(z)$ (5) greenhouse gas forcings (GHG) due to CO_2 , CH_4
 525 and N_2O changing as a function of time t and $f(X(t), \epsilon, \theta, \nu)$ is the clear sky radiative
 526 transfer equation for channel center frequency ν . The spectral noise $NeDT(\nu)$ for a typ-
 527 ical tropical “clear scene” is about 0.1 K in window region, increasing to about 1 K in
 528 the $15 \mu m$ temperature sounding channels and about 0.2 K in the $6.7 \mu m$ water vapor
 529 sounding region, but the noise will vary as a function of scene temperature. We parametrize
 530 the GHGs using single numbers (such as ppm(t) for the CO_2 column), and include the
 531 AIRS orbit and viewing angle geometry θ and the surface emissivity $\epsilon(\nu)$, while we omit
 532 forward model and spectroscopy errors. We ignore cloud scattering as well as the spa-
 533 tial variation of the state parameters, emissivity and scan angle geometry within a tile.
 534 Linearizing the above equation about the time averaged profile, the relationship between
 535 the observed spectral trends and desired thermodynamic trends is given by

$$\frac{d\overline{BT(\nu)}}{dt} = \frac{\partial f}{\partial \overline{X}} \frac{d}{dt} \overline{X(t)} = K(\nu) \frac{d}{dt} \overline{X(t)} + \cancel{K_{\text{emissivity}}(\nu) \frac{d}{dt} \epsilon(t)} \xrightarrow{0} K(\nu) \frac{d}{dt} \overline{X(t)} \quad (4)$$

536 where the matrix $K(\nu)$ is the thermodynamic jacobian (surface temperature, air
 537 temperature and trace gases) and we ignore any orbit drifts (changes to θ), instrument
 538 changes (changes to $NeDT(\nu)$) and surface emissivity ($\epsilon(\nu)$); the last assumption is in-
 539 vestigated in a later section. The overbars on parameters X denotes this is a time ave-
 540 rage (linear trend) that we are working with, and we have converted from radiances in
 541 Equation 2 to brightness temperatures in Equations 3 and 4.

542 6.2 Jacobian calculations

543 For a typical clear sky tropical sky atmosphere, the $800 - 1200 \text{ cm}^{-1}$ window re-
 544 gion has surface temperature (SKT) jacobians which are about $+0.5$ to $+0.75 \text{ K per de-}$
 545 $gree SKT$ change and -0.75 to $-0.25 \text{ K per 10\% change in column water vapor}$. The spec-
 546 tral variability in these window region jacobians is primarily due to reducing water con-
 547 tinuum absorption as you move from the 800 cm^{-1} end to the 1200 cm^{-1} ; consequently
 548 the surface temperature jacobians becomes closer to unity and the column water jaco-
 549 bians become closer to zero as water vapor amount decreases (drier atmospheres in the
 550 mid-latitudes and polar regions). The hyperspectral channels used in this work assist in
 551 partitioning these two competing changes (though not perfectly), which we validate against
 552 other datasets in this study. As seen in Figure 4 typical magnitudes of the spectral trends
 553 on the left hand side of Equation 4 are less than about 0.1 K per year. Equation 4 is in

554 the usual inversion form $\delta y = K\delta x$, and the Optimal Estimation (Rodgers, 2000) so-
 555 lution used to solve the anomaly time series in Strow et al. (2021) is also used here. The
 556 noise term used for the trend retrieval $NeDT(\nu)$ is not the instrument noise since each
 557 16 day point in our time series is averaged over hundreds of observations as earlier de-
 558 scribed; instead the uncertainty is that due to inter-annual variability in the linear trends
 559 obtained from the trend fitting in Equation 2. Examples of typical noise values are shown
 560 in the bottom right hand panel of Figure 3.

561 ERA5 monthly model fields at tile centers, together with time varying concentra-
 562 tions of GHG such as CO₂, were averaged over 20 years so jacobians could be computed.
 563 The GHG concentrations were a latitude dependent increase of about 2.2 ppm yr⁻¹ for
 564 CO₂ derived from the CarbonTracker Peters et al. (2007) (CarbonTracker CT-NRT.v2023-
 565 4, <http://carbontracker.noaa.gov>) model data at 500 mb. Our pseudo-monochromatic
 566 line by line code kCARTA De Souza-Machado et al. (2018, 2020) was used with these av-
 567 eraged profiles to produce accurate analytic jacobians. The HITRAN 2020 line param-
 568 eter database Gordon and Rothman (2022), together with MT-CKD 3.2 and CO₂,CH₄
 569 line mixing from the LBLRTM suite of models Clough et al. (2005) were used in the kCARTA
 570 optical depth database De Souza-Machado et al. (2018). A 12 month geographical land-
 571 varying spectral emissivity database spanning one year from Zhou et al. (2011) was used,
 572 while ocean emissivity came from Masuda et al. (1988). The atmospheric temperature,
 573 water vapor and ozone profile jacobians, and the surface temperature and column jaco-
 574 bians for the GHG gases such as CO₂ and CH₄ and N₂O, were then convolved using the
 575 best estimate AIRS Spectral Response Functions Strow, Hannon, Weiler, et al. (2003).

576 Tests done for this paper, together with the results in Strow et al. (2021), estab-
 577 lished that jacobians derived from MERRA2 versus ERA5 produced no significant dif-
 578 ferences in the context of retrieved trends or anomalies done for this paper, as the un-
 579 certainty in linear trends due to inter-annual variability dominates over any uncertainty
 580 (or differences between) model fields.

581 **6.3 Optimal Estimation Retrieval : State vector, covariance matrices** 582 **and *a-priori***

583 Using monthly ERA5 model fields averaged over 20 years, for each of the 64×72
 584 tiles we computed analytic jacobians for the following (vector) atmospheric thermody-
 585 namic variables [fractional water vapor, fractional ozone and temperature] together with
 586 (scalar) surface temperature. We retrieved fractional gas concentration trends $dfrac{X}/dt =$
 587 $1/X_{avg}(z)dX_{avg}(z)/dt$ to keep all values in the state vector at about the same magni-
 588 tude. A single iteration Optimal Estimation retrieval Rodgers (2000) is used to simul-
 589 taneously solve for the geophysical parameter trends. As in (Strow & DeSouza-Machado,
 590 2020) the geophysical covariance uncertainty matrices are a combination of Tikonov and
 591 covariance regularization. The uncertainties for the covariance matrices were typically
 592 [0.1,0.25,0.45] K yr⁻¹ for the surface/tropospheric/stratospheric temperature trends, and
 593 [0.04/0.02] yr⁻¹ for the fractional tropospheric/stratospheric water vapor trends. Tikonov
 594 L1 regularization (Rodgers, 2000) also included, with the scalar factor multiplying this
 595 regularization corresponding to about 1/10 the covariance uncertainties. The spectral
 596 uncertainties used in the retrievals come from the above mentioned trend uncertainties.
 597 For completeness we note that a sequential retrieval (see for example Smith and Bar-
 598 net (2020)) produces very similar geophysical trends.

599 Here we emphasize four points about our geophysical trend retrievals, which sets
 600 us apart from trends derived from other datasets. Firstly the *a-priori* trend state vec-
 601 tor is zero ($dST/dt = dT(z)/dt = dQ(z)/dt = 0$) for all geophysical parameters, except
 602 for water vapor where we enforced constant (or slightly increasing) relative humidity as
 603 described below. This ensures traceability of our retrieval is straightforward especially
 604 wherever the AIRS instrument has sensitivity. For example the 300 - 800 mb water va-

605 por trend retrievals will be based on the data only, thereby insulating us from any possible
 606 *a-priori* information from *e.g.* climatology or NWP models, unlike the operational
 607 AIRS V7 or CLIMCAPS retrievals which use first guesses based on neural net and MERRA2
 608 respectively.

609 Secondly as seen in Figures 4 and 5, in the 15 μm region there is a large spectral
 610 overlap signal (-0.06 K yr^{-1}) from the increasing CO_2 , which is much larger than the
 611 expected atmospheric temperature trend (0.01 K yr^{-1}). These correlations makes it dif-
 612 ficult to jointly retrieve both temperatures changes and changes in well mixed GHGs such
 613 as CO_2 . We chose to focus on retrieving temperature changes only, by spectrally remov-
 614 ing the effects of changing CO_2 , CH_4 and N_2O GHG concentrations. This was done by
 615 using the GHG trends estimated from NOAA ESRL CarbonTracker data multiplied by
 616 the appropriate GHG gas column jacobian ($\text{CO}_2, \text{N}_2\text{O}$ and CH_4 and CFC11, CFC12) com-
 617 puted as described above using the averaged over 20 years ERA5 monthly profile for each
 618 tile.

619 Thirdly instead of using all 100 layers described in the AIRS forward model Strow,
 620 Hannon, DeSouza-Machado, et al. (2003), we combine pairs of layers for a 50 atmospheric
 621 layer retrieval, as the AIRS radiances contain far fewer than 100 pieces of information
 622 (see *e.g.* Maddy and Barnet (2008); De Souza-Machado et al. (2018)).

623 Fourthly, modern hyperspectral infrared sounders have highest sensitivity to tem-
 624 perature and water vapor in the mid-tropopause; see for example the averaging kernels
 625 in Irion et al. (2018). Using a zero fractional WV trends *a-priori* at all levels, it was fairly
 626 straightforward to obtain fractional $\text{WV}(z)$ trends close to those from the NWP model
 627 datasets in the 300-850 mb region. In order to improve our results in the lowest layers,
 628 we enforced a constant relative humidity approximation, which is a well-known, expected
 629 behavior under global climate change Soden and Held (2006); Sherwood et al. (2010).
 630 This was done by ignoring the contribution due to water vapor changes in the observed
 631 BT1231 trend, and using it as an approximation for air temperature trend over ocean;
 632 this allows us to compute an estimate of how the water vapor would need to change

$$RH(T) = \frac{e}{e_{sat}(T)} \implies \delta(RH) = \frac{1}{e_{sat}(T)} \delta e - \frac{e}{e_{sat}^2(T)} \delta e_{sat}(T) = \frac{1}{e_{sat}(T)} \delta e - \frac{e}{e_{sat}(T)} \frac{L_v}{R_v} \frac{1}{T^2} \delta T \quad (5)$$

633 where $e, e_{sat}(T)$ are the vapor pressures and we used $e_{sat}(T) = e_{s0} e^{\frac{L_v}{R_v} (\frac{1}{T_0} - \frac{1}{T})}$ (where
 634 L_v, R_v are latent heat of vaporization and gas constant respectively) to go from the ex-
 635 pression in the center to the expression on the right. If we expect the change in RH to
 636 be zero then $\frac{\delta e}{e} = \frac{L_v}{R_v} \frac{\delta T}{T^2}$, where we can use $\delta T / \delta t \sim d/dt BT1231$. to approximate the
 637 *a-priori* fractional vapor pressure rates (or *a-priori* fractional water vapor rates) between
 638 surface and 850 mb, smoothly tailing to 0 in the upper atmosphere. Subsection 7.2 has
 639 a similar discussion on a proposed method to alleviate the lack of sensitivity to upper
 640 atmosphere water vapor. Our default results in this paper are from using the MLS *a-*
 641 *priori*, unless otherwise stated.

642 **6.4 Testing on synthetic trend spectra made from ERA5 Reanalysis monthly** 643 **fields**

644 We tested the retrieval code by using it on the simulated nighttime only ERA5 spec-
 645 tral trends, and compared to geophysical trends computed directly from the ERA5 re-
 646 analysis model. Spot checks of the spatial correlations of ERA5 fractional water vapor
 647 and temperature trends versus the trends retrieved from synthetic spectra/our retrieval
 648 algorithm, peaked at 500 mb with correlations of about 0.9, compared to 800 mb cor-
 649 relations of 0.80 and 0.55 for temperature and fractional water vapor trends respectively
 650 and 200 mb correlations of 0.89 and 0.69 for $dT/dt, d\text{WVfrac}/dt$. This is to be expected
 651 since a computation of the water vapor averaging kernels for infrared instruments for ar-
 652 bitrary atmospheric profiles typically shows they peak in the 300 mb - 850 mb range and

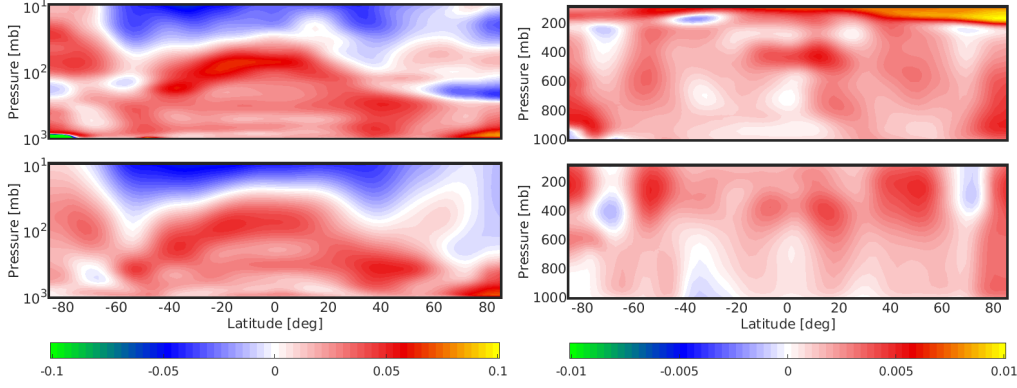


Figure 6. Comparing geophysical trends derived directly from ERA5 monthly nighttime fields (top) vs from the AIRS_RT retrieval applied to the ERA5 reconstructed spectral trends (bottom). Left panel is dT/dt (in $K\ yr^{-1}$) while rightmost panel is $d(\text{fracWV})/dt$ (colorbar in yr^{-1}).

653 decrease rapidly away from those regions; conversely the temperature averaging kernels
 654 stay relatively uniform through the free troposphere and above, though they also decrease
 655 close to the surface; see for example Irion et al. (2018); Smith and Barnett (2020); Wu
 656 et al. (2023).

657 Figure 6 shows a sample set of results using nighttime ERA5 model output converted
 658 to spectral trends as described above. The top panels (A) are always the atmospheric
 659 trends computed directly from the monthly ERA5 model fields, while the bottom pan-
 660 els (B) are the atmospheric trends retrieved from the converted ERA5 spectral bright-
 661 ness temperature trends. The left most panel is the atmospheric temperature trend com-
 662 parison (both in $K\ \text{yr}^{-1}$) while the rightmost panel is the fractional atmospheric water
 663 vapor trend comparison (in yr^{-1}).

664

665 It is evident from the figure that the tropospheric trends in the tropical and mid-
 666 latitude regions are quite similar, and there are differences in the polar regions and strato-
 667 spheric regions where the AIRS instrument has reduced sensitivity. The atmospheric and
 668 surface trends are shown in Table 1, divided into “all” (which is the entire ± 90 latitude
 669 range and 0-1000 mb vertical range) and “T/M” which is the tropical/midlatitude region,
 670 which is further reduced to 050-900 mb for air temperature and 300-800 mb for water
 671 vapor. “ERA5 direct” are trends computed directly from the geophysical fields, while “ERA5
 672 spectral” are retrieved from the spectral trends.

673 6.5 Surface emissivity changes

674 Equation 3 explicitly includes the surface emissivity in the equation of radiative
 675 transfer; however Equation 4 assumes this is unchanging. Here we rewrite Equation 4
 676 as

$$\frac{d\overline{BT}(\nu)}{dt} - K_{\text{emissivity}}(\nu) \frac{d}{dt} \overline{\epsilon(t)} \rightarrow \frac{d\overline{BT}(\nu)}{dt} = K(\nu) \frac{d}{dt} \overline{X(t)} \quad (6)$$

677 Ocean emissivity has a dependence on windspeed Masuda et al. (1988). Lin and
 678 Oey (2020) and other literature suggest wind speed increases of $+2.5\ \text{cm}\ \text{s}^{-1}\ \text{yr}^{-1}$ have
 679 occurred between 1993-2015 in the tropical Pacific, and smaller (or close to zero) values

	dTz/dt K yr ⁻¹ A SFC-TOA	dTz/dt K yr ⁻¹ T/M 050-900 mb	dSKT/dt K yr ⁻¹ A	dSKT/dt K yr ⁻¹ T/M	dfracWV/dt K yr ⁻¹ A GND-TOA	dfracWV/dt K yr ⁻¹ T/M 300-800 mb
ERA5 direct	0.010 ± 0.038	0.029 ± 0.013	0.020 ± 0.035	0.018 ± 0.032	0.003 ± 0.002	0.002 ± 0.001
ERA5 spectral	0.004 ± 0.033	0.027 ± 0.012	0.019 ± 0.033	0.016 ± 0.029	0.001 ± 0.001	0.002 ± 0.001

Table 1. Cosine weighted air temperature, skin temperature, fractional water vapor trends, together with uncertainties. The “ERA5 direct” are directly from the ERA5 geophysical trends, while “ERA5 spectral” are trends retrieved from the converted ERA5 spectral trends.

680 elsewhere. The monthly ERA5 $u10,v10$ 10 m speeds for the 20 year time period in this
681 paper also showed the maximum absolute trend was 0.09 m/s/year (over the Southern
682 Ocean) while the global ocean mean and standard deviation were 0.006 ± 0.022 m s⁻¹
683 yr⁻¹; The emissivity changes over ocean using a 0.025 m s⁻¹ wind speed change are on
684 average on the order of 1×10^{-6} per year in the thermal infrared window (or about 0.0003
685 K yr⁻¹ change in the window region); assuming the optical properties of water do not
686 substantially change with the ~ 0.02 K increases seen in all the datasets considered in
687 this paper, these very small emissivity changes are of no consequence.

688 Land emissivity changes were estimated as follows. A global monthly mean emis-
689 sivity database, the Combined ASTER and MODIS Emissivity over Land (CAMEL v003)
690 has recently been released Borbas et al. (2018). We matched the tile centers to the database
691 for the 20×12 months spanning our 2002/09 - 2022/08 time period, and computed the
692 emissivity trends over land; the results (not shown here) were on the order of -1×10^{-4}
693 and $+3 \times 10^{-4}$ in the 800-960 cm⁻¹ and 1100-1250 cm⁻¹ regions respectively, averaged
694 over the land observations. For each tile the $K_{emissivity}(\nu) \frac{d}{dt} \epsilon(t)$ term was estimated by
695 running SARTA with the default emissivity, then differencing with the SARTA output
696 obtained when the emissivity trends were added on. Averaged over the planet, the spec-
697 tral changes arising from these emissivity changes were much smaller than the spectral
698 trends seen in Figure 3, about -0.001 K yr⁻¹ between 800-960 cm⁻¹ and about +0.002
699 K yr⁻¹ on the 1100-1250 cm⁻¹ region (which we do not use in our retrieval, since many
700 of the channels are synthetic and the real channels are drifting (Strow et al., 2021)). The
701 land only results were roughly three times these magnitudes. Using these emissivity ja-
702 cobians on the left hand side of Equation 6 and running the retrieval on the adjusted spec-
703 tral trends over land, resulted in about at most 0.01 K increases to the zonally averaged
704 surface temperature changes over land; zonally averaged these largest differences were
705 at about 40°N to 60°N and -25°S to +15°N, due to emissivity decreases; the 20°N to
706 +35°N region which included the Sahara and swathes of Asia, had emissivity increases
707 but the averaged-over-land temperature decreases were small, as there were offsetting
708 emissivity increases in other land areas at the same latitudes. We did not pursue the im-
709 pact of these emissivity changes further as the CAMEL database is affected by the sta-
710 bility of the MODIS data, and our results below will not include accounting for changes
711 in land emissivity.

712 7 Results

713 The trends retrieved in the previous section using simulated radiance trends show
714 that the retrieval package is working as expected. Here we apply our retrieval to observed
715 AIRS L1C radiance trends and compare the retrieved AIRS_RT geophysical trends to
716 those computed directly from the ERA5/MERRA2 model fields and AIRS L3/CLIMCAPS
717 L3 products. We will have an expectation that since the simulated radiance trends had

718 no noise added to them, the uncertainty in the spectral rates was lower than the actual
 719 observed spectral uncertainty; this will lead to larger uncertainties and/or errors in our
 720 retrieval using observed radiance trends.

721 We will make most comparisons against NWP models and L3 products in the con-
 722 text of averages over the descending/night (N) and ascending/day (D) data since the MERRA2
 723 (and GISS) datasets are only available as a D/N average; the reader is referred to the
 724 Appendix where we show a few of the D-N differences. The results are shown in the or-
 725 der of surface/column trends (surface temperature and column water), followed by zonal
 726 averages of the atmospheric temperature and fractional water vapor trends.

727 7.1 Skin Temperature trends

728 There are typically multiple (window) channels that are sensitive to a surface pres-
 729 sure, meaning the radiances typically have more information content for the surface tem-
 730 perature (assuming the surface emissivity is well known and there are no clouds) rather
 731 than for example air temperature. Figure 7 shows the diurnally averaged day/night (D/N)
 732 surface temperature trends from 6 datasets : AIRS_RT, AIRS L3, CLIMCAPS L3, ERA5,
 733 MERRA2 and NASA GISTEMP. AIRS_RT shows an overall global warming of $+0.021$
 734 K yr^{-1} ; the cooling trends include the tropical eastern Pacific and south of Greenland
 735 and tropical northern Atlantic. The rest of the datasets also show similar patterns of cool-
 736 ing in the N. Atlantic Ocean, warming over the Arctic and some degree of cooling over
 737 the Antarctic Ice Shelf/Southern Ocean as does AIRS_RT. The AIRS v7 L3 shows some
 738 cooling over Central Africa and the Amazon not seen in the AIRS_RT trends, where
 739 one could expect Deep Convective Clouds and possible cloud clearing issues. We also point
 740 out the AIRS L3 product has many missing values off the western coasts of N. and S.
 741 America, due to cloud clearing issues. MERRA2 shows more cooling over C. Africa, and
 742 just like the AIRS v7 data, a lot of cooling near the Antarctic Ice Shelf. Of note here
 743 is that although CLIMCAPS uses MERRA2 as its first guess, their surface temperature
 744 trends are not similar, especially around the Antarctic where MERRA2 shows strong cool-
 745 ing trends. Over the ocean GISS shows similar trends to what AIRS_RT trends show.
 746 An earlier study of Land Surface Temperatures between 2003-2017 using MODIS Prakash
 747 and Norouzi (2020) shows very similar large daytime cooling trends over parts of cen-
 748 tral and western Indian subcontinent that we see from our retrieval as well as directly
 749 from the BT1231 channel trends; for tiles that straddle both ocean and land the quan-
 750 tile method picks up the hottest observations, which especially during summer are mostly
 751 over the Indian subcontinent. For these reasons we also have confidence in our retrieved
 752 cooling trends over for example daytime continental Central/Eastern Africa, which are
 753 different from the other four day/night datasets.

754
 755 The spatial correlations between AIRS_RT retrieved rates and the various datasets
 756 is shown in Table 2 while the cosine weighted skin temperature trends are shown in Ta-
 757 ble 3. By adding in the uncertainty in the trends for any of the individual models or datasets,
 758 and then doing the cosine weighting, we estimate uncertainties of about $\pm 0.015 \text{ K yr}^{-1}$
 759 for “ALL”; the uncertainties for “OCEAN” are typically about 2/3 of that value, and for
 760 “LAND” are about 4/3 of that value. We emphasize here that we use center point NWP
 761 and L3 model data when computing their trends for any grid box, while the AIRS_RT
 762 uses the hottest 10% of “clear” data; Strow and DeSouza-Machado (2020) showed that
 763 the tropical retrieved surface temperature trends and anomalies over ocean correlated
 764 very well with those from the ERA-I Sea Surface Temperature dataset.

765 A notable outlier in this group is the MERRA2 trends, especially over land and
 766 the Southern Ocean which are noticeably negative (blue) compared to the other datasets;
 767 the agreement with tropical and mid-latitude oceans is much better. As noted earlier,

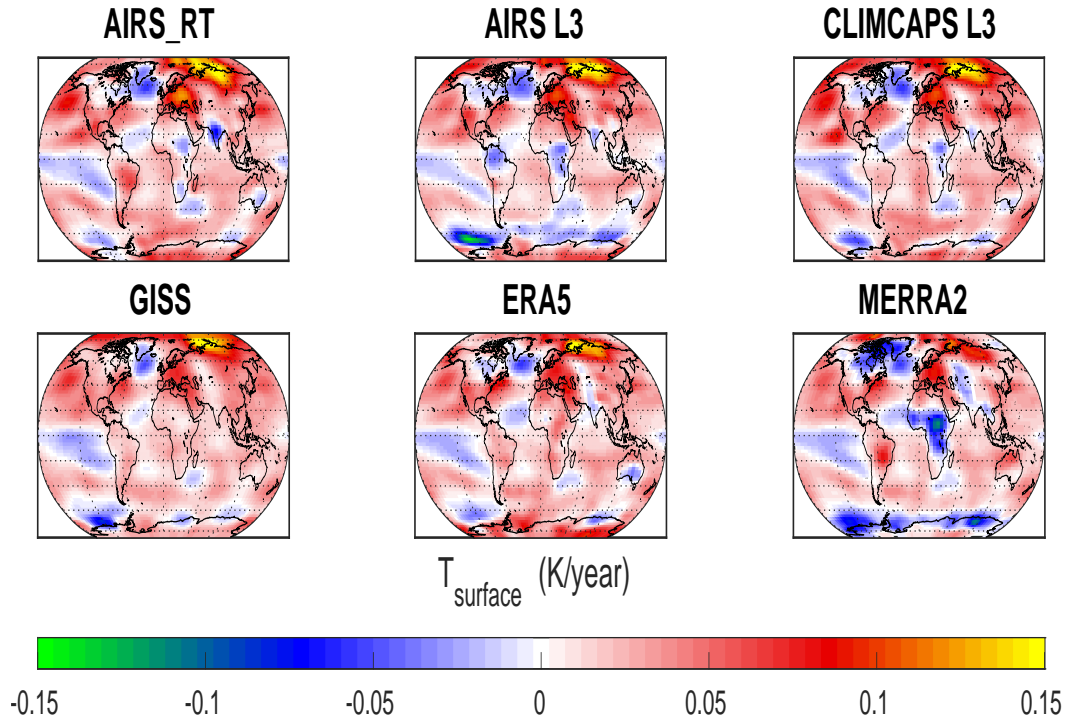


Figure 7. Surface temperature trends $d\text{SKT}/dt$ averaged over day and night for AIRS_RT, and from separately fitting the monthly data in ERA5, MERRA2, AIRS L3, CLIMCAPS L3 and GISS.

ERA5	MERRA2	AIRSL3	CLIMCAPSL3	GISS
0.72	0.59	0.80	0.89	0.77

Table 2. Correlations of average (nighttime, daytime) retrieved skin temperature trends from AIRS_RT, versus trends from models/products

768 the MERRA2 monthly trends come from a combination day/night dataset that was down-
 769 loaded, which as seen in Figure 7 consists of trends that are both positive and negative,
 770 combining to get a closer-to-zero global weighted trend. In addition MERRA2 is the only
 771 one of the six that (a) does not have the extreme $+0.15 \text{ K yr}^{-1}$ warming in the north-
 772 ern polar region and (b) shows a lot of cooling in the Central African area. Using ERA5
 773 monthly data, we devised a test similar to the one mentioned in Section 5 to determine
 774 if the differences between MERRA2 and ERA5 surface temperature trends could be due
 775 to the temporal sampling (once for MERRA2 versus eight times for ERA5). For each
 776 month we matched the eight ERA5 timesteps available per month to the tile centers and
 777 then averaged the surface temperatures per month; the ensuing geophysical timeseries
 778 was then trended. The day/night ERA5 average of Figure 7 was compared to these trends;
 779 of note are (a) we did not see the cooling in Africa and near the Antarctic that is seen
 780 in MERRA2 and (b) the main differences between the 1.30 am/1.30 pm average in the
 781 bottom middle (ERA5) panel were over land (all 5 continents); the histograms of the dif-
 782 ferences showed the peak was typically close to 0 K yr^{-1} , but the widths over land were
 783 about $\pm 0.02 \text{ K yr}^{-1}$ or less (compared to $\pm 0.005 \text{ K yr}^{-1}$ over ocean). Both AIRS L3
 784 and MERRA2 show cooling in the Southern Ocean; we note that although MERRA2 is
 785 the *a-priori* for CLIMCAPS L3, their trends are different that those from MERRA2; in

SKT trend K yr^{-1}	AIRS_RT	AIRS	CLIMCAPS	ERA5	MERRA2	GISS
ALL	0.020	0.017	0.021	0.023	0.011	0.021
TROPICS	0.011	0.011	0.012	0.016	0.010	0.015
MIDLATS	0.029	0.020	0.028	0.026	0.020	0.026
POLAR	0.032	0.028	0.033	0.041	-0.005	0.028
OCEAN	0.019	0.011	0.019	0.017	0.012	0.017
LAND	0.022	0.030	0.024	0.038	0.010	0.030

Table 3. Cosine weighted skin temperature trends; uncertainties are on the order of $\pm 0.015 \text{ K}$ as explained in the text.

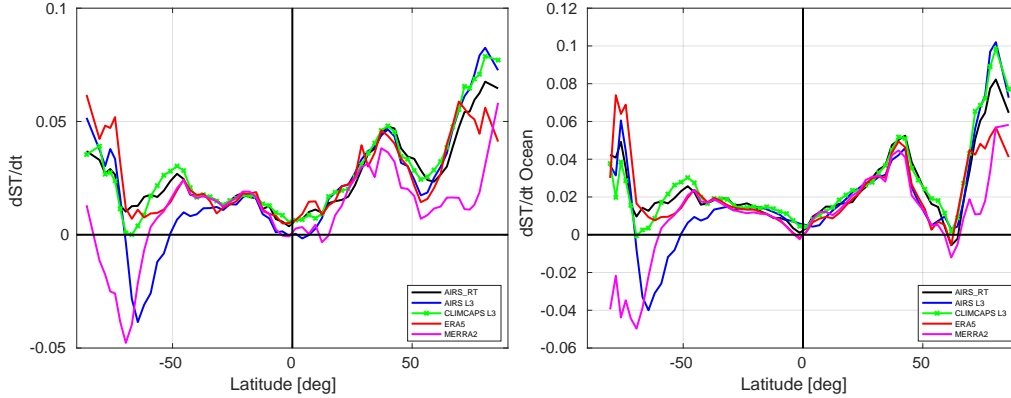


Figure 8. Zonally averaged surface temperature trends for (left) sum of ocean and land point and (right) ocean only.

786 fact AIRS_RT shows the closest correlation to the observational CLIMCAPS L3 trends.
 787 The AIRS L3 trends in the Southern Ocean region could arise because of problems identifying ice during the L2 retrieval (private communication : Evan Manning (JPL) and
 788 John Blaisdell (NASA GSFC)) though the MERRA2 trends also show significant cooling in that region, where few surface observations from buoys poleward of 60° exist to
 789 help resolve these differences (see for example Figure 10 in Haiden et al. (2018)).
 790
 791

792 Figure 8 shows the zonally averaged total (land+ocean) and ocean only surface temperature trends. The equator to midlatitude ocean trends are almost linear for all datasets,
 793 with the slope for the northern hemisphere being about double that of the southern hemisphere (roughly 0.001 K yr^{-1} per deg latitude). Again focusing on the right hand plot,
 794 the AIRS L3 trends are negative in the Southern Ocean regions, compared to the other 3 datasets, due to the cooling trends around the Antarctic continent shown earlier, but
 795 then agrees with most of the other datasets over the Antarctic; the MERRA2 trends significantly differ between -90 S and -50 S . MERRA2 and ERA5 also show slightly smaller
 796 warming trends in the Northern Polar, compared to the three AIRS-based datasets.
 797
 798
 799
 800

801
 802 We point out that the trends seen in Figure 7 vary noticeably at more local, regional
 803 levels and furthermore this spatial variation can differ between daytime and nighttime,
 804 evident in Figure A1 of Appendix Appendix A, and that the observational sets (AIRS_RT,

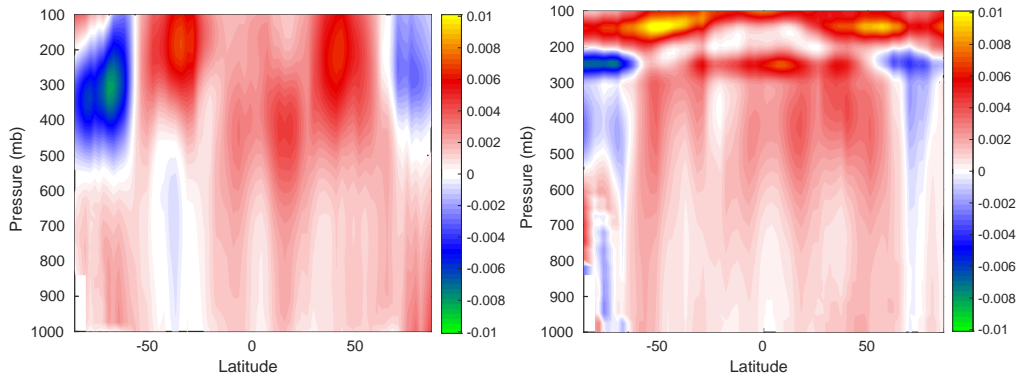


Figure 9. $dWVfrac/dt$ (left) without and (right) with MLS *a-priori* in the upper atmosphere

805 CLIMCAPS L3 and AIRS L3) had larger differences than ERA5. Discussing the possible
 806 causes is outside the scope of the paper.

807 **7.2 Addition of Microwave Limb Sounder Water Vapor A-priori**

808 The Microwave Limb Sounder (MLS), on board NASA's Aura platform, is designed
 809 for sounding of the atmosphere above 300 mb. We computed water vapor trends from
 810 the L3 data produced for that instrument (above 300 mb) and used them as an *a-priori*
 811 for the AIRS_RT retrieval.

812

813 Figure 9 shows the retrieved fractional water vapor trends when the *a-priori* trend
 814 in the upper atmosphere in the left and right panels were zero, or used MLS trends, re-
 815 spectively. One sees that the additional information brought in by the instrument sen-
 816 sitive to upper troposphere humidity, significantly changes the water vapor sounding es-
 817 pecially in the polar region by moving towards the MERRA2 and ERA5 fractional wa-
 818 ter vapor trends seen in Figure 12. We note that the other related results shown in this
 819 paper use the MLS *a-priori*.

820 **7.3 Column water vapor trends**

821 Column water is dominated by water vapor amounts close to the surface and the
 822 column vapor trends thus provide an assessment of the water vapor retrieval quality in
 823 the lower atmosphere. The water vapor information in the lowest layers is best retrieved
 824 using the weak water lines in thermal infrared region. As noted earlier this part of the
 825 retrieval is significantly complicated by the simultaneous presence of nonzero surface tem-
 826 perature, air temperature and water vapor jacobians in this spectral region, meaning the
 827 AIRS instrument has much reduced sensitivity to the water vapor amounts in these low-
 828 est layers. In addition the changing concentration of very minor gases such as CFC-11
 829 and CFC-12 Strow and DeSouza-Machado (2020) are quite evident in the spectral trends,
 830 further complicating the water vapor trend retrieval for the lowest layers.

831

832 Figure 10 shows the zonally averaged column water vapor trends; not shown are
 833 the error bars which are on the order of ± 0.005 mm/year. AIRS_RT is from our re-
 834 trievals while the rest are directly from the NWP or L3 model fields. Close examination

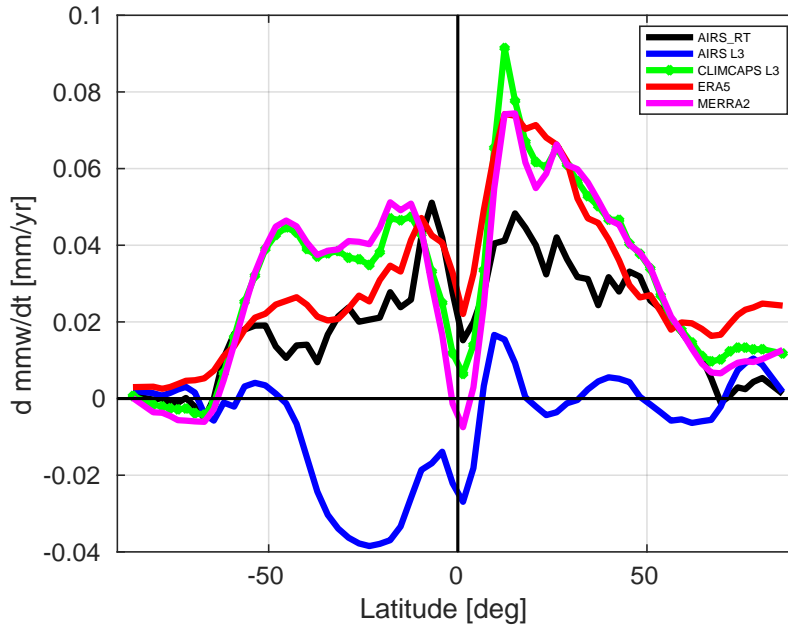


Figure 10. Zonally averaged column water vapor trends for AIRS_RT, AIRS L3, CLIMCAPS L3, ERA5 and MERRA2.

835 shows the CLIMCAPS L3 column water trend is nearly identical to the MERRA2 trend,
 836 as is also seen in lower atmosphere water vapor trends shown later in Figure 12. Con-
 837 versely the column water vapor trends for AIRS L3 are negative in the lower troposphere
 838 in the midlatitudes and tropics, which is not to be expected given that the surface tem-
 839 perature trends are positive. AIRS_RT nominally agrees with ERA5 and MERRA2 in
 840 the tropics and midlatitudes, but is smaller than either in the northern polar regions.
 841 A reduced rate for AIRS_RT is additionally seen in the 0-50 N latitudes, where there
 842 is a larger fraction of land (for which we do not use the assumption of constant relative
 843 humidity) compared to the Southern Hemisphere. Screening out the tiles over land slightly
 844 improves the agreement between reanalysis (ERA5, MERRA2) vs AIRS_RT column wa-
 845 ter trends. Examination of the spectral trends in the window region does not shed any
 846 more insight into the differences, as the observation spectral trends and NWP reconstructed
 847 trends are very similar and we are fitting the observed trends. The magnitudes and pat-
 848 terns look similar to the 2005-2021 column water trends shown in Borger et al. (2022),
 849 which were derived using observations from the Ozone Monitoring Instrument (OMI).
 850 We point out their 16 year zonally averaged trends look similar to the 20 year ERA5 zon-
 851 ally averaged column water trends between -60°S and -10°S , but become almost a fac-
 852 tor of 2 larger between -10°S and $+40^{\circ}\text{N}$; the zonally averaged OMI 16 year trends are
 853 negative in the polar regions. The column water trends are summarized in Table 4.

854 D/N differences (not shown) for AIRS_RT were on the order of $\pm 0.005 \text{ mm yr}^{-1}$
 855 (with daytime trends being smaller over land), for AIRS L3 were on the order of ± 0.01
 856 mm yr^{-1} or more (with larger values happening over the daytime tropical oceans), while
 857 that for ERA5 and CLIMCAPS L3 were typically on the order of $\pm 0.03 \text{ mm yr}^{-1}$ or
 858 less.

859 7.4 Zonal atmospheric temperature and water vapor trends

860

DATASET mm yr ⁻¹	OMI 16 years	AIRS_RT 20 years	ERA5 20 years	MERRA2 20 years	AIRS L3 20 years	CLIMCAPS L3 20 years
GLOBAL (cosine average)	0.051	0.021	0.035	0.036	-0.009	0.038
TROPICAL	0.083	0.028	0.047	0.042	-0.015	0.045

Table 4. Column water trends based on OMI data (16 years) and AIRS_RT, ERA5 and MERRA2 (20 years). The units are in mm yr⁻¹; the uncertainties are on the order of 0.1 mm yr⁻¹ for OMI and AIRS_RT, and half that for ERA5 and MERRA2, and AIRS L3 and CLIMCAPS L3.

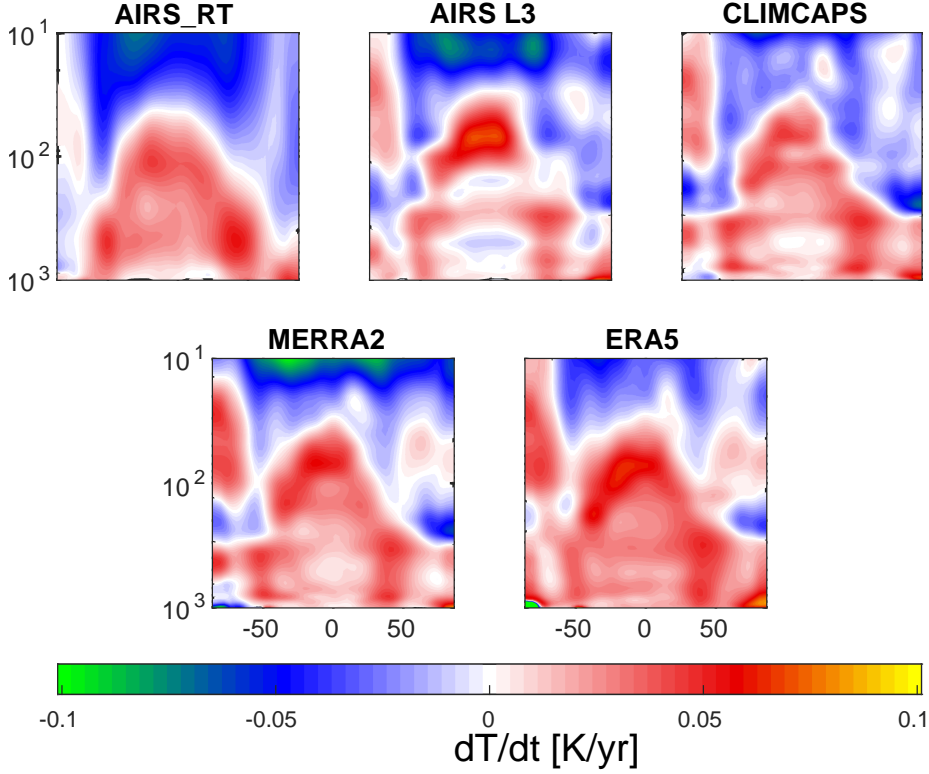


Figure 11. Zonally averaged dT/dt shown in 5 panels. Horizontal axis is latitude while vertical axis is pressure. The y -limits are between 10 to 1000 mb, on a logarithmic scale.

861 Figure 11 shows the zonally averaged atmospheric temperature trends from five of
 862 the datasets in Figures 7,10 above. In the troposphere the AIRS_RT retrievals show the
 863 same general features as the trends from ERA5, though they begin to diverge in the strato-
 864 sphere and especially above that. In particular AIRS_RT does not show warming in the
 865 Southern Polar stratosphere; we have separately looked into seasonal trends and noted
 866 that our retrieved September/October/November temperature trends in the upper at-
 867 mospheric Southern Polar regions are on the order of -0.12K yr^{-1} , possibly leading to
 868 an overall no net heating/cooling for the annual trends. In addition we point out that
 869 both our results and AIRS v7 L3 show a hint of cooling over the tropical surfaces. Note
 870 that CLIMCAPS is initialized by MERRA2, and their temperature trends are quite sim-
 871 ilar. AIRS v7 looks similar to AIRS_RT except in the tropics where it almost has cool-
 872 ing in the lower troposphere and much more warming in the lower stratosphere. The cor-
 873 relations between AIRS_RT and the [AIRS L3, CLIMCAPS L3, MERRA2, ERA5] tem-
 874 perature trends of Figure 11 are [0.74,0.65,0.74,0.72] respectively.

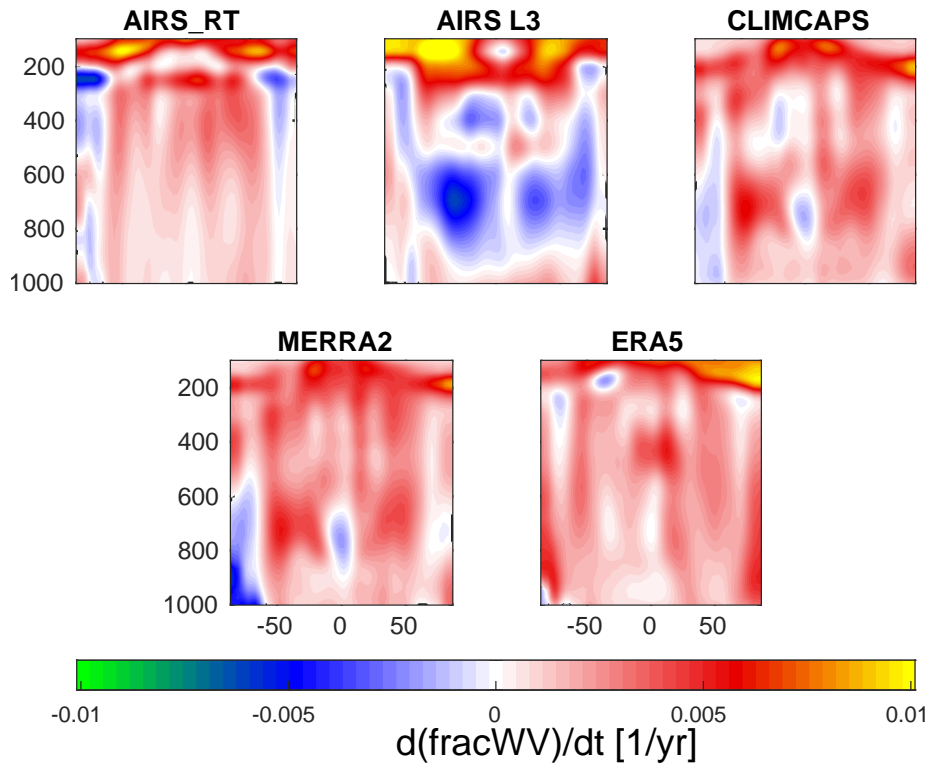


Figure 12. Zonally averaged dWV_{frac}/dt shown in 5 panels. Horizontal axis is latitude while vertical axis is pressure. The y -limits are between 100 to 1000 mb, on a linear scale.

875

876 Figure 12 shows the zonally averaged atmospheric fractional water vapor trends
 877 ($d/dt \text{ WV}(z,t)/\langle \text{WV}(z,t) \rangle$). The five panels are markedly different from one another.
 878 The AIRS_RT trends resemble those of ERA5 in the tropical troposphere, though we
 879 do not have drying in the lower tropical layers. Conversely, the observed trends in the
 880 Southern Polar (AIRS L3, CLIMCAPS L3 and AIRS_RT) show drying rather than wet-
 881 ting, though AIRS_RT is less than that of CLIMCAPS/MERRA2. AIRS_RT is an out-
 882 lier in the upper polar atmosphere trends, as both the signals and the jacobians are close
 883 to zero. Of some concern is a little bit of drying in the northern polar region, where there
 884 are low H_2O amounts leading to small jacobians. CLIMCAPS v2 looks quite similar to
 885 the MERRA2 trends. AIRSv7 shows substantial drying in the lower troposphere, and
 886 considerable wetting in the upper troposphere, compared to any of the other datasets.
 887 Spectral closure studies (using the AIRS v7 H_2O trend \times the H_2O jacobians derived above
 888 from ERA5 average profiles) are not shown here, but differ noticeably from the CCR trends
 889 from AIRS v7 in the $1300\text{-}1600 \text{ cm}^{-1}$ region, indicating there are inadequacies in the AIRS
 890 V7 water vapor retrievals. The correlations between AIRS_RT and the [AIRS L3, CLIM-
 891 CAPS L3, MERRA2, ERA5] fractional water vapor trends of Figure 12 (limited to 100
 892 mb, 1000 mb) are [0.65,0.24,0.36,0.58] respectively.

893 Figure 13 shows the 400 mb fractional water vapor trends, with the left panel be-
 894 ing the AIRS_RT trends while the right panel is the ERA5 trends. Note that there is
 895 general agreement except in the Southern Polar region, as also seen later in Figure 12
 896 in the other two observational L3 datasets (AIRS v3 and CLIMCAPS). This could be
 897 related to work by Boisvert et al. (2019) who showed decreasing evaporation from the
 898 Southern Ocean in the 2003-2016 period due to increasing ice cover.

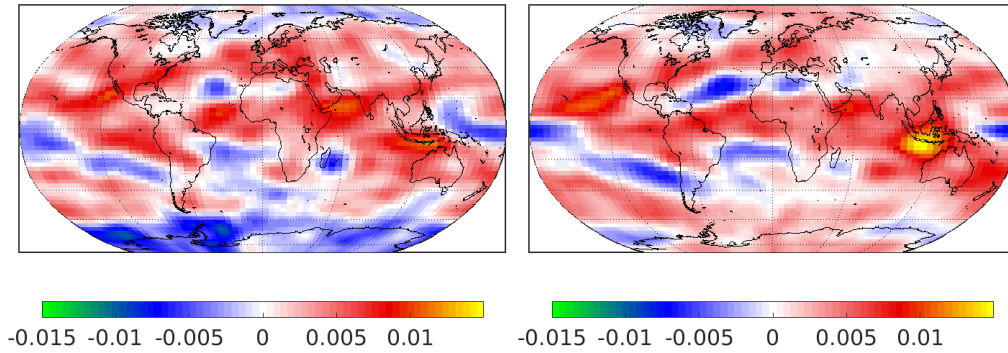


Figure 13. The 400 mb fractional water vapor trends for (left) AIRS_RT and (right) ERA5 show general agreement except in the Southern Polar Regions.

899

900 8 Uncertainty

901 The uncertainties for the AIRS v7 geophysical products are impacted by radiance
 902 noise amplification due to cloud clearing Susskind et al. (2003) and the neural net first
 903 guess, while state vector errors are estimated based on regressions. CLIMCAPS L2 geo-
 904 physical products are similarly impacted by cloud clearing noise in the radiances, but
 905 these are fully propagated together with geophysical error estimates from the MERRA2
 906 first guess, through the retrieval algorithm which uses Optimal Estimation Smith and
 907 Barnett (2020). No estimate of uncertainties are available for the monthly L3 products.

908 The uncertainties for the AIRS_RT trends is much more straightforward : the spec-
 909 tral uncertainties shown in Figure 4 are used together with the state vector covariance
 910 matrices to generate the uncertainty matrix using the relevant equations of Optimal Es-
 911 timation (Rodgers, 2000); we use the diagonal elements for the final uncertainties. Pan-
 912 els (A) and (C) of Figure 14 shows the zonally averaged (D/N) uncertainties as a func-
 913 tion of pressure and latitude. Inspection of the radiance trends uncertainties shown in
 914 the center panel of Figure 4 shows the upper atmosphere temperature sounding region
 915 ($650\text{-}700\text{ cm}^{-1}$) has much larger uncertainty in the polar regions. The instrument and
 916 spectroscopy characteristics, coupled with these observational uncertainties, are such that
 917 for temperature the smallest errors are in the tropics while the largest errors are in pol-
 918 ar upper atmosphere, which are the regions below 100 mb where the ERA5 trends dif-
 919 fer most from AIRS_RT trends. Similarly for water vapor the larger errors are in the
 920 lower atmosphere and above about 300 mb; the constant RH assumption and MLS *a-*
 921 *priori* help alleviate the errors in the retrieved trends.

922 The *Z-test* confirmed this picture, as seen in panels (B) and (D) of Figure 14, which
 923 show the temperature and fractional water vapor trends, together with black dots mark-
 924 ing the (latitude,altitude) points where the trends are larger than the uncertainty in the
 925 trends, at the 5% significance level. This happens in panel (B) for the temperature trends
 926 in most of the tropical/mid-latitude free troposphere (and stratosphere) but not at the
 927 southern polar stratosphere; and in panel (D) for fractional water vapor trends in the
 928 200-600 mb range, from the Southern Polar region to about +60 N latitude, and some
 929 spots in the Northern Polar.

930

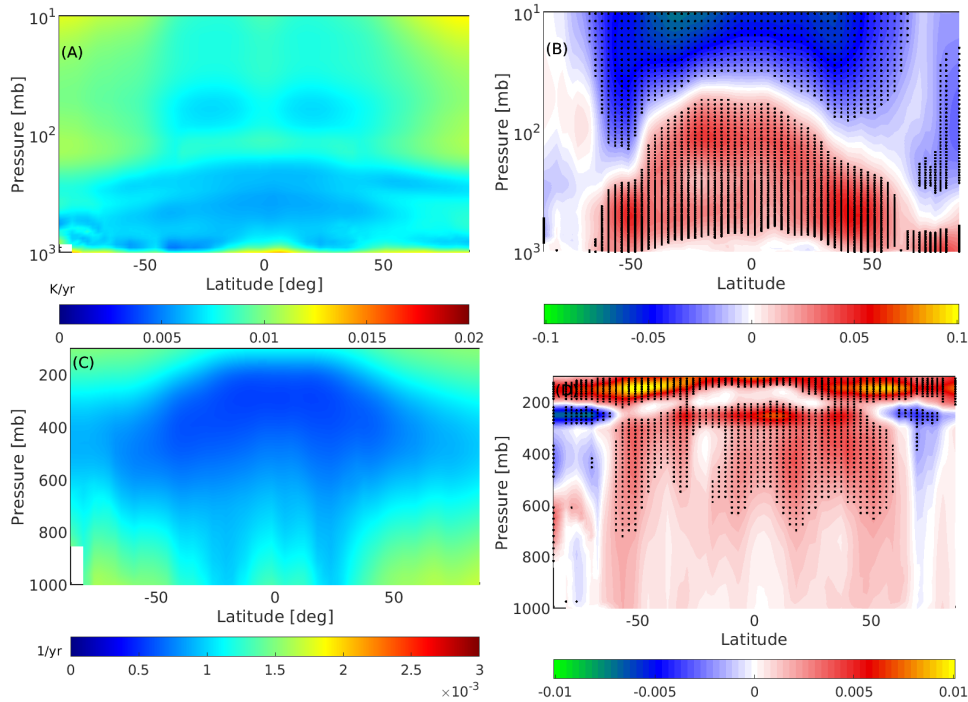


Figure 14. Zonally averaged D/N plots of (A) temperature uncertainties in K yr^{-1} and (B) temperature trends in K yr^{-1} together with null hypothesis. (C) and (D) are the same except for fractional water vapor uncertainty and trends in $1/\text{year}$. See text for more detailed explanation.

931

9 Discussion

932

933

934

935

936

937

938

939

940

941

942

943

944

In general for surface temperature trends, the disagreements between the six sets shown in Figure 7 are over the polar regions and over land (especially over the Amazon and Central Africa) and are smallest over tropical and mid-latitude oceans, indicating the best agreements, except for slightly larger differences off the western coast of the Americas and Africa (which have a prevalence of MBL clouds). The atmospheric temperature trends in general agreed except for the upper atmosphere polar regions and in the high altitudes (less than about 200 mb). Similarly fractional water vapor trends differed most in the upper atmosphere (200 mb and above) and in the tropical/mid-latitude 600-800 mb region. A quick glance at Figure 12 shows the former is due to lower sensitivity to upper atmosphere water vapor, leading the AIRS_RT retrievals to have low values while the AIRS L2 retrieval is initialized by a neural net; conversely the latter is due to the AIRS L3 retrieval being negative while the rest were mainly positive. Similarly the AIRS_RT retrieval differs above the Antarctic continent.

945

946

947

948

949

950

951

952

In general the observed surface temperature trends from the AIRS_RT retrievals agree with the ERA5 and MERRA2 trends, as well as the NASA GISS trends, except in the Southern Antarctic. That is a region where there are few surface observations; for retrievals there are competing effects of using ice vs ocean surface emissivity. Overall, the AIRS_RT retrieved surface temperature trends are typically in between ERA5 and MERRA2 for land + ocean in all regimes (tropical, midlatitude and polar), though slightly larger overall for ocean than the two reanalysis datasets; in general they are closer to the ERA5 trends than the MERRA2 trends.

953

954

Stow et al. (2021) demonstrated that the long- and medium- wave channels of the AIRS instrument are radiometrically stable to better than $0.002\text{-}0.003 \text{ K yr}^{-1}$, which is

955 much smaller than the surface and tropospheric temperature trends in the reanalysis mod-
 956 els, AIRS L3 data and our retrieved trends. A separate analysis of spectral trend un-
 957 certainties after 05,10,15,20 years (not shown here) show that these uncertainties have
 958 been steadily decreasing and are now approaching this number, as can be seen in the bot-
 959 tom left panel of Figure 3. Furthermore, though we cannot guarantee only cloud free scenes
 960 in our chosen Q0.90 dataset used in this paper, the high correlations between other dataset
 961 surface trends compared to ours, is a good indication that our results come from mostly
 962 cloud-free scenes, or scenes whose clouds have negligible impact on our results.

963 The observed zonal temperature trends agree with those from the models and the
 964 AIRS L3 products, except in the polar regions. Again this could be an issue of using slightly
 965 incorrect surface emissivity for the AIRS_RT retrievals. In addition we point out that
 966 since there is very little water vapor, the temperature jacobians near the surface are quite
 967 small in magnitude (compared to more humid atmospheres) and so it is difficult to sep-
 968 arate out the effects of surface temperature trends versus lower atmosphere temperature
 969 and H₂O trends. The quantile construction used in this paper means that for example
 970 tiles straddling the subcontinent of India and the ocean will preferentially pick the land
 971 surface observations for daytime, which could lead to misleading trends on these coastal
 972 tiles. It is possible to subdivide the $3^\circ \times 5^\circ$ tiles into for example $1^\circ \times 1^\circ$ grids and do the
 973 analysis, but the number of observations per small grid cell would drop, leading to more
 974 noise in the retrieved trend.

975 In general the AIRS_RT retrieved absolute column water trends are slightly smaller
 976 than ERA5 in the Southern Hemisphere but noticeably smaller in the Northern Trop-
 977 ics to midlatitudes. We have mentioned difficulties we have retrieving H₂O close to the
 978 surface and in the upper atmosphere, due to the known sensitivity of infrared sounders
 979 whose water vapor averaging kernels peak in the 300-600 mb range, and we have pointed
 980 out examination of the spectral residuals in the window region shows we are fitting the
 981 signal. The MERRA2 and CLIMCAPS column water vapor trends are quite similar, while
 982 the AIRSv3 L3 trends are noticeably different, being negative almost everywhere.

983 Given the complex numerical algorithms used in both the reanalysis models and
 984 the AIRS L3 retrievals as well as those in the AIRS_RT trends, it is difficult to offer pre-
 985 cise explanations for any of the trends shown above. Our results are relatively robust
 986 to changes in the covariance or Tikonov parameter settings. For instance changing them
 987 by factors of two would keep the trends about the same, though of course the uncertain-
 988 ties would change. There are however a few general points that can be made. The first
 989 is that since infrared instruments are sensitive to the 300-800 mb region and lose sen-
 990 sitivity outside this, the retrievals from AIRS_RT and AIRS L3 have difficulties with
 991 water vapor in the lower (Planetary Boundary Layer) and upper troposphere/lower strato-
 992 sphere. One way to mitigate this is to use trended data from external sources in the *a-*
 993 *priori*, while keeping the *a-priori* trends for all other parameters as 0. For example we
 994 have shown we can use the MLS data above 300 mb without significantly degrading the
 995 AIRS_RT retrieval in the middle and lower atmosphere; conversely the CLIMCAPS re-
 996 trievals are initialized by MERRA2 and while they can pull out weather signals, their
 997 L3 trends are still quite closely tied to the MERRA2 trends. The tropical and mid-latitude
 998 ocean surface temperature trends from the numerical models that assimilate data, L3
 999 products and AIRS_RT are very similar; however they start to show differences where
 1000 there are few *in-situ* data combined with problems with ice identification (surface emis-
 1001 sivity)/cold temperatures which exacerbate the drifting AIRS detector problems Strow
 1002 et al. (2021), such as the Arctic and Southern Ocean.

1003 10 Conclusions

1004 We have described a novel method to obtain global thermodynamic atmospheric
 1005 climate trends, starting from infrared allsky hyperspectral observations which are then

1006 subset for “nominally clear” scenes. Our retrieved trends are derived using trends from
 1007 well characterized (radiometrically stable) radiances and from zero *a-priori* (except for
 1008 a constant relative humidity assumption). This makes them much more direct and trace-
 1009 able than trends from traditional L2 retrieval algorithms, which use complicated *a-priori*
 1010 information. We also did “radiative closure” tests by running the monthly NWP or L3
 1011 fields through a radiative transfer model to compare the spectral trends so obtained against
 1012 the observed spectral trends, which showed the most disagreement in the water vapor
 1013 sounding regions.

1014 The temperature and water vapor trends retrieved from the “nominally clear” ra-
 1015 diance trends resemble those computed from monthly ERA5 and MERRA2 reanalysis.
 1016 The radiative spectral closure helps identify the cause of differences in the geophysical
 1017 trends, rather than solely attributing them to deficiencies (eg the well known reduced
 1018 sensitivity to water vapor near the boundary layer and above 200 mb) with our retrieval.
 1019 For example the AIRS_RT temperature trends are quite similar to the reanalysis (MERRA2/ERA5)
 1020 trends, while the water vapor (and/or Relative Humidity) trends are quite different, es-
 1021 pecially in the lower troposphere and upper troposphere, which is clearly manifest as dif-
 1022 ferences in the spectral trends in the water vapor sounding region.

1023 The 20 years of AIRS observations were binned into nominal 3×5 degree grid boxes
 1024 covering the planet, with a time step of 16 days, from which anomalies and trends were
 1025 obtained. To alleviate the reduced sensitivity of hyperspectral sounders to water vapor
 1026 in the lower atmosphere we used an assumption of 0.01 increase in relative humidity to
 1027 initialize the *a-priori* lower atmosphere fractional water vapor rates, while we similarly
 1028 used Microwave Limb Sounder trends as an *a-priori* to address the high altitude water
 1029 vapor deficiencies caused by lower sensitivity to upper atmosphere water vapor. New or
 1030 updated time dependent surface emissivity databases may become available in the fu-
 1031 ture, enabling us to include those effects into Equation 4. Problems in the polar regions
 1032 and Planetary Boundary Layer water vapor retrievals will be harder to overcome since
 1033 there is very little sensitivity to water vapor in these regions, together with fewer obser-
 1034 vations to compare against, though more work is planned to address both of these.

1035 In this paper we used the 90th quantile (Q0.90) nominally “hottest” observed BT1231
 1036 data to form a time series over which to obtain radiance trends, after establishing that
 1037 the spectral trends from this quantile differed by less than about $\pm 0.0015 \text{ K yr}^{-1}$ from
 1038 the 50th (or average) quantile. In the future we plan to base the data subset selection
 1039 on MODIS cloud products (obtained at 1 km resolution compared to the AIRS 15 km
 1040 resolution). In any case the AIRS LIC Q0.90 spectral trends used for the AIRS_RT re-
 1041 sults are very comparable to trends from quality assured binned AIRS CCR data Manning
 1042 (2022). The quantile method allows us to select which data to use in the trends : we have
 1043 explored doing the trend retrievals using the cloud fields contained in ERA5, together
 1044 with the TwoSlab cloud algorithm De Souza-Machado et al. (2018) to compute jacobians
 1045 when clouds are present, together with trends from the Q0.50 dataset described above.
 1046 The retrieved geophysical trends resemble those described above in the mid to upper at-
 1047 mosphere, and differ in the lower atmosphere, but more work is needed on this and is
 1048 not discussed further. Longwave clear sky flux trends (both outgoing top-of-atmosphere
 1049 and incoming bottom-of-atmosphere) and climate feedbacks will be discussed in a sep-
 1050 arate paper.

1051 While the Aqua platform is scheduled to be terminated within the next few years,
 1052 copies of near identical CrIS instruments are already in orbit, and more will be launched
 1053 over the next few years, till at least 2040. The Climate Hyperspectral Infrared Radiance
 1054 Product (CHIRP) Strow et al. (2021) will seamlessly combine the AIRS data between
 1055 2002-2015 to CrIS data from 2015-2040 to obtain a 40 year observational radiance record
 1056 over which to study climate. This availability means that AIRS_RT and future AIRS/CrIS
 1057 versions, is well positioned to enable climate analysis of geophysical trends for years to
 1058 come.

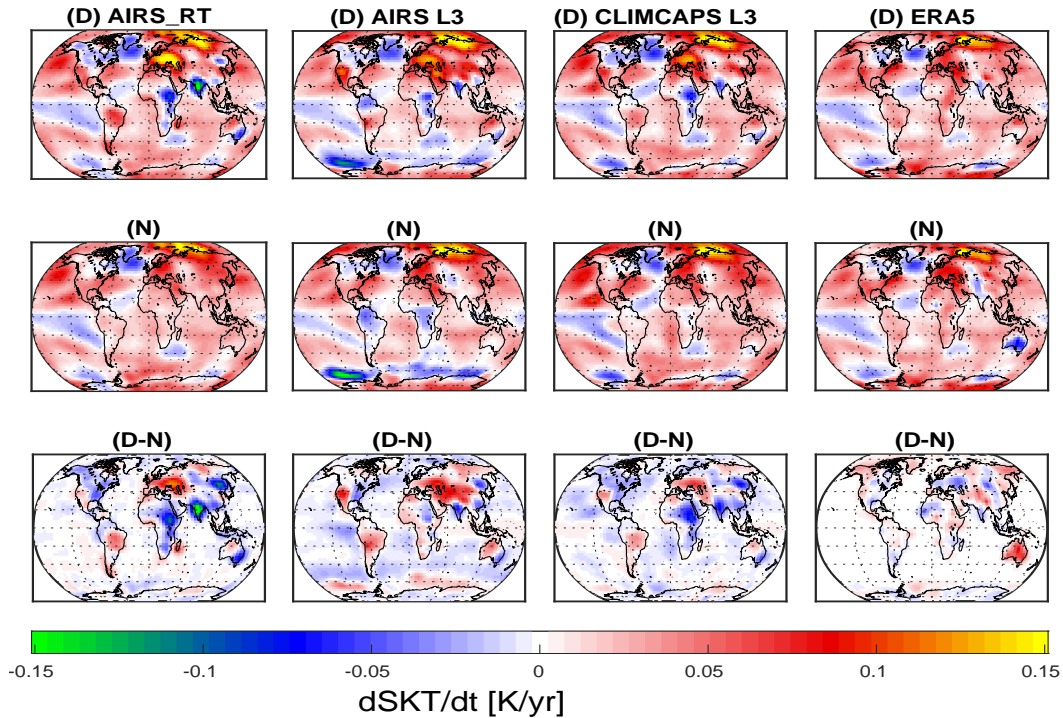


Figure A1. Top two rows : The (top) day and (middle) night surface temperature trends for AIRS_RT, AIRS L3, CLIMCAPS L3 and ERA5. Third row (bottom) is the D-N difference.

Appendix A Day versus Night surface temperature trend differences

Figure A1 shows the (top) daytime and (middle) nighttime surface temperature trends; from left to right the datasets are (observational) AIRS_RT, AIRS L3, CLIMCAPS L3 and (reanalysis) ERA5. In general the AIRS observational datasets show enhanced daytime cooling over the Indian subcontinent and Central Africa, compared to the ERA5 model; they also show daytime warming trends over continental Europe and central Asia and the Amazon are larger than during the nighttime. With the large ocean heat capacity and smaller land heat capacity, the land is expected to show more of a diurnal cycle than ocean. ERA5 sees warming over Eastern/Central Africa during daytime while the observational datasets see cooling. Similarly the three observational datasets see more daytime cooling over the Indian sub-continent and south eastern Australia than does ERA5; we omit more detailed analysis in this paper. During the nighttime, the AIRS L3 product has cooling over C. Africa and parts of the Amazon. The day-night differences are seen in the bottom row of the same figure. Note the colorbar is the same for all three rows. The differences are close to zero over the ocean. AIRS_RT and CLIMCAPS L3 see more daytime cooling over E. Africa and the Indian subcontinent. Overall the magnitude of the day - night differences for the observations are larger for the AIRS observational datasets than for ERA5. ERA5 also sees negative differences over Central Asia compared to the AIRS observational datasets, which see positive differences (higher surface temperature trends during the daytime).

The atmospheric temperature and fractional water vapor day-night differences are quite small (compared to the average values) and not shown here; AIRS L3 shows no-

1082 ticeable more wetting of the 600-800 mb region during daytime versus nighttime, com-
1083 pared to the other three.

1084 **Data Availability Statement**

1085 The observation data used in this paper (AIRS L1C radiances), as well as the AIRS
1086 L3, CLIMCAPS L3, MERRA-2 and Microwave Limb Sounder monthly data products,
1087 are freely available to the public on the NASA Goddard Space Flight Center Earth Sci-
1088 ences (GES) Data and Information Services Center (DISC) servers <https://disc.gsfc.nasa.gov/>.
1089 Monthly ERA5 is freely available through (single levels) [https://cds.climate.copernicus.eu/](https://cds.climate.copernicus.eu/datasets/reanalysis-era5-single-levels-monthly-means?tab=overview)
1090 [datasets/reanalysis-era5-single-levels-monthly-means?tab=overview](https://cds.climate.copernicus.eu/datasets/reanalysis-era5-single-levels-monthly-means?tab=overview) and (pressure lev-
1091 els) [https://cds.climate.copernicus.eu/datasets/reanalysis-era5-pressure-levels-monthly-](https://cds.climate.copernicus.eu/datasets/reanalysis-era5-pressure-levels-monthly-means?tab=overview)
1092 [means?tab=overview](https://cds.climate.copernicus.eu/datasets/reanalysis-era5-pressure-levels-monthly-means?tab=overview). GISTEMP monthly model output are also freely available from
1093 <https://data.giss.nasa.gov/gistemp/>. The Matlab based source code used for the anal-
1094 ysis is freely available on https://github.com/sergio66/oem_climate_code, while the F90
1095 kCARTA De Souza-Machado et al. (2018) line-by-line code used to make the jacobians
1096 is freely available on https://github.com/sergio66/kcarta_gen.

1097 **Acknowledgments**

1098 We gratefully acknowledge the help of H. Motteler, who designed, implemented and
1099 ran the AIRS tiling code. C. Hepplewhite helped test the outputs of the tiling code, S.
1100 Buczkowski worked on bringing down almost all the data used in this study, and made
1101 the uniform/clear datasets. Chris Barnet has given helpful comments and general ad-
1102 vice regarding retrievals and comparisons to the AIRSv7 and CLIMCAPS datasets. The
1103 hardware used is part of the UMBC High Performance Computing Facility (HPCF). The
1104 facility is supported by the U.S. National Science Foundation through the MRI program
1105 (grant nos. CNS-0821258, CNS-1228778, OAC-1726023, and CNS-1920079) and the
1106 SCREMS program (grant no. DMS-0821311), with additional substantial support from
1107 the University of Maryland, Baltimore County (UMBC). See hpcf.umbc.edu for more
1108 information on HPCF and the projects using its resources.

1109

References

- 1110 2023, G. T. (2005). *GISS Surface Temperature Analysis (GISTEMP), version 4*
 1111 (Tech. Rep.). data accessed 2023/11/30 at <https://data.giss.nasa.gov/gistemp/>:
 1112 NASA Goddard Institute for Space Studies.
- 1113 Boisvert, L., Vihma, T., & Shie, C.-L. (2019). Evaporation From the South-
 1114 ern Ocean Estimated on the Basis of AIRS Satellite Data. *JGR*, *125*,
 1115 <https://doi.org/10.1029/2019JD030845>.
- 1116 Borbas, E., Hulley, G., Feltz, M., Knuteson, R., & Hook, S. (2018). The Com-
 1117 bined ASTER MODIS Emissivity over Land (CAMEL) Part 1: Method-
 1118 ology and High Spectral Resolution Application. *Remote Sens.*, *10*, 643;
 1119 <https://doi.org/10.3390/rs10040643>.
- 1120 Borger, C., Beirle, S., & Wagner, T. (2022). : Analysis of global trends of total
 1121 column water vapour from multiple years of OMI observations. *Atmos. Chem.*
 1122 *Phys.*, *22*, 10603–10621, <https://doi.org/10.5194/acp-22-10603-2022>.
- 1123 Clough, S., Shephard, M., Mlawer, E., Delamere, J., Iacono, M. J., Cady-Pereira,
 1124 K., ... Brown, P. (2005). Atmospheric radiative transfer modeling : a
 1125 summary of the AER codes. *J. Quant. Spectrosc. Rad. Trans.*, *91*, 233-
 1126 244doi:10.016/j.qsrt2004.05.058.
- 1127 De Souza-Machado, S., Strow, L. L., Motteler, H., & Hannon, S. (2020). kCARTA :
 1128 A Fast Pseudo Line by Line Radiative Transfer Algorithm with Analytic Jaco-
 1129 bians, Fluxes, Non-Local Thermodynamic Equilibrium and Scattering. *Atmos.*
 1130 *Meas. Tech.*, *31*, 323–339, <https://doi.org/10.5194/amt-13-323-2020>.
- 1131 De Souza-Machado, S., Strow, L. L., Tangborn, A., Huang, X., Chen, X., Liu, X.,
 1132 ... Yang, Q. (2018). Single-footprint retrievals for AIRS using a fast TwoSlab
 1133 cloud-representation model and the SARTA all-sky infrared radiative transfer
 1134 algorithm. *Atmos. Meas. Tech.*, *11*, 529-550,[https://doi.org/10.5194/amt-11-](https://doi.org/10.5194/amt-11-529-2018)
 1135 529-2018.
- 1136 Gelaro, R., & Coauthors. (2017). MERRA-2 Overview: The Modern-Era Retrospec-
 1137 tive Analysis for Research and Applications, Version 2 (MERRA-2). *J. Clim.*,
 1138 *30*, 5419-5454, doi: 10.1175/JCLI-D-16-0758.1.
- 1139 Gordon, I., & Rothman, L. e. a. (2022). The HITRAN 2020 molecular
 1140 spectroscopic database. *J. Quant. Spectrosc. Rad. Trans.*, *277*, 1-
 1141 82,<https://doi.org/10.1016/j.jqsrt.2021.107949>.
- 1142 Haiden, T., Dahoui, M., Ingleby, B., de Rosnay, P., Prates, C., Kuscü, E., ... Jones,
 1143 L. (2018). *Use of in situ surface observations at ECMWF* (No. 834).
- 1144 Hersbach, H., Bell, B., Berrisford, P., Hirahara, S., Horányi, A., Muñoz-
 1145 Sabater, J., ... Thépaut, J.-N. (2020). The ERA5 Global Reanalysis.
 1146 *Quart. J. Roy. Meteorol. Soc.*, *146*, 1999-2049,<https://doi.org/10.1002/qj.3803>.
- 1147 Huang, X., Chen, X., Fan, X., Kato, S., Loeb, N., Bosilovich, M.,
 1148 ... Strow, L. (2023). A Synopsis of AIRS Global-Mean
 1149 Clear-Sky Radiance Trends From 2003 to 2020. *JGR*, *127*,
 1150 e2022JD037598.<https://doi.org/10.1029/2022JD037598>.
- 1151 Irion, F., Kahn, B., Schreier, M., Fetzer, E., Fishbein, E., Fu, D., ... Yue, Q. (2018).
 1152 Single-footprint retrievals of temperature, water vapor and cloud properties
 1153 from AIRS. *Atmos. Meas. Tech.*, *11*(2), [https://doi.org/10.5194/amt-11-971-](https://doi.org/10.5194/amt-11-971-2018)
 1154 2018.
- 1155 King, M., Platnick, S., Menzel, P., Ackerman, S., & Hubanks, P. (2013). Spatial and
 1156 Temporal Distribution of Clouds Observed by MODIS Onboard the Terra and
 1157 Aqua Satellite. *IEEE*, *51*, 3826-3852,10.1109/TGRS.2012.2227333.
- 1158 Lambert, A., Read, W., Livesey, N., & Fuller, R. (2021). *MLS/Aura Level 3 Monthly*
 1159 *Binned Vapor (H2O) Mixing Ratio on Assorted Grids V005* (Tech. Rep.).
 1160 https://disc.gsfc.nasa.gov/datasets/ML3MBH20_005/summary: NASA
 1161 Greenbelt, MD, USA, Goddard Earth Sciences Data and Information Services
 1162 Center (GES DISC).
- 1163 Lenssen, N., Schmidt, G., Hansen, J., Menne, M., Persin, A., Ruedy, R., & Zys, D.

- 1164 (2019). Improvements in the GISTEMP uncertainty model. *JGR*, *124*(12),
 1165 6307-6326, doi:10.1029/2018JD029522.
- 1166 Lin, Y., & Oey, L. (2020). Global Trends of Sea Surface Gravity Wave, Wind, and
 1167 Coastal Wave Setup. *J. Clim.*, *33*, 769–785, <https://doi.org/10.1175/JCLI-D-19-0347.1>.
 1168
- 1169 Maddy, E., & Barnett, C. (2008). Vertical Resolution Estimates in Ver-
 1170 sion 5 of AIRS Operational Retrievals. *IEEE*, *66*(8), 2375-2384, DOI
 1171 10.1109/TGRS.2008.917498.
- 1172 Manning, E. (2022). *Nasa jpl private communication, 4/2022*. (AIRS CCR L3 data)
- 1173 Manning, E., Aumann, H., Broberg, S., Pagano, T., Wilosn, R., Yanovsky, I.,
 1174 & Strow, L. (2020). *Eos airs 11c data product user guide* (Tech. Rep.).
 1175 https://docserver.gesdisc.eosdis.nasa.gov/public/project/AIRS/V6.7_L1C_Product_User_Guide.pdf.
 1176 NASA.
- 1177 Masuda, K., Takashima, T., & Takayama, Y. (1988). Emissivity of pure and sea wa-
 1178 ters for the model sea surface in the infrared window regions. *Remote Sensing*
 1179 *of Environment*, *24*, 313–329.
- 1180 Palchetti, L., Brindley, H., Bantges, R., Buehler, S. A., Camy-Peyret, C., Carli, B.,
 1181 ... Serio, C. (2020). FORUM: unique far-infrared satellite observations to
 1182 better understand how Earth radiates energy to space. *Bull.Amer.Met.Soc.*,
 1183 *101*, <https://doi.org/10.1175/BAMS-D-19-0322.1>.
- 1184 Peters, W., Jacobson, A., Sweeney, C., & Tans, P. (2007). An atmospheric perspec-
 1185 tive on North American carbon dioxide exchange: CarbonTracker. *Proc. Nat.*
 1186 *Aca. Sci.*, *104*, 18925-18930, <https://doi.org/10.1073/pnas.0708986104>.
- 1187 Prakash, S., & Norouzi, H. (2020). Land surface temperature variability across In-
 1188 dia: a remote sensing satellite perspective. *Theor. Appl. Climatol.*, *139*, 773-
 1189 784, <https://doi.org/10.1007/s00704-019-03010-8>.
- 1190 Raghuraman, S., Paynter, D., V., R., & Menzel, R. H. X. (2023). Green-
 1191 house Gas Forcing and Climate Feedback Signatures Identified in Hy-
 1192 perspectral Infrared Satellite Observations. *Geophys. Res. Lett.*, *50*,
 1193 <https://doi.org/10.1029/2023GL103947>.
- 1194 Rodgers, C. (2000). Inverse Methods for Atmospheric Sounding. In (p. 256 pages).
 1195 World Scientific, Singapore.
- 1196 Roemer, F., Buehler, S., Brath, M., Kluft, L., & John, V. (2023). Direct observation
 1197 of Earth’s spectral long-wave feedback parameter. *Nature Geoscience*, *16*, 416-
 1198 421, <https://doi.org/10.1038/s41561-023-01175-6>.
- 1199 Sherwood, S., Ingram, W., Tshushuma, Y., Satoh, M., Roberts, M., Vidale, P., &
 1200 O’Gorman, P. (2010). Relative humidity changes in a warmer climate. *J.*
 1201 *Geophys. Res.*, *115*, <https://doi.org/10.1029/2009JD012585>.
- 1202 Smith, N., & Barnett, C. (2019). Uncertainty Characterization and Propa-
 1203 gation in the Community Long-Term Infrared Microwave Combined At-
 1204 mospheric Product System (CLIMCAPS). *Remote Sensing*, *11*, 1227-
 1205 1251, doi:10.3390/rs11101227.
- 1206 Smith, N., & Barnett, C. (2020). CLIMCAPS observing capability for temperature,
 1207 moisture, and trace gases from AIRS/AMSU and CrIS/ATMS. *AMT*, *13*,
 1208 4437–4459, <https://doi.org/10.5194/amt-13-4437-2020>.
- 1209 Smith, N., & Barnett, C. (2023). Practical Implications of CLIMCAPS Cloud
 1210 Clearing and Derived Quality Metrics. *Earth Space Sci*, *10*, e2023EA002913.
 1211 <https://doi.org/10.1029/2023EA002913>.
- 1212 Soden, B., & Held, I. (2006). An assessment of climate feedbacks in coupled ocean-
 1213 atmosphere models. *J. Clim*, *19*, 3354-3360.
- 1214 Strow, L., & DeSouza-Machado, S. (2020). Establishment of AIRS climate-level
 1215 radiometric stability using radiance anomaly retrievals of minor gases and sea
 1216 surface temperature. *Atmos. Meas. Tech.*, *13*, <https://doi.org/10.5194/amt-13-4619-2020>.
 1217
- 1218 Strow, L., Hannon, S., DeSouza-Machado, S., Tobin, D., & Motteler, H. (2003).

- 1219 An overview of the AIRS radiative transfer model. *IEEE Transactions on*
 1220 *Geosciences and Remote Sensing*, 41, 303-313.
- 1221 Strow, L., Hannon, S., Weiler, M., Overoye, K., Gaiser, S., & Aumann, H. (2003).
 1222 Pre-launch spectral calibration of the Atmospheric InfraRed Sounder (AIRS).
 1223 *IEEE Transactions on Geosciences and Remote Sensing*, 41, 274-286.
- 1224 Strow, L., Hepplewhite, C., Motteler, H., Buczkowski, S., & DeSouza-Machado, S.
 1225 (2021). A Climate Hyperspectral Infrared Radiance Product (CHIRP) Com-
 1226 bining the AIRS and CrIS Satellite Sounding Record. *Rem. Sens.*, 13(3),
 1227 <https://doi.org/10.3390/rs13030418>.
- 1228 Susskind, J., Barnet, C., & Blaisdell, J. (2003). Retrieval of atmospheric and sur-
 1229 face parameters from AIRS/AMSU/HSB data under cloudy conditions. *IEEE*
 1230 *Transactions on Geosciences and Remote Sensing*, 41, 390-409.
- 1231 Susskind, J., Blaisdell, J., & Iredell, L. (2014). Improved methodology for surface
 1232 and atmospheric soundings, error estimates, and quality control procedures:
 1233 the Atmospheric Infrared Sounder science team version-6 retrieval algorithm.
 1234 *J. App. Rem. Sens.*, 8(1), 084994 [10.1117/1.JRS.8.084994].
- 1235 Tian, B., E. M., Roman, J., Thrastarson, H., & Fetzer, R., E. ad Monarrexz.
 1236 (2020). *Airs version 7 level 3 product user guide* (Tech. Rep.). Jet
 1237 Propulsion Laboratory, California Institute of Technology. Retrieved from
 1238 [https://docserver.gesdisc.eosdis.nasa.gov/public/project/AIRS/](https://docserver.gesdisc.eosdis.nasa.gov/public/project/AIRS/V7_L3_User_Guide.pdf)
 1239 [V7_L3_User_Guide.pdf](https://docserver.gesdisc.eosdis.nasa.gov/public/project/AIRS/V7_L3_User_Guide.pdf)
- 1240 Whitburn, S., Clarisse, L., Bouilon, M., Safieddine, S., George, M., Dewitte, S.,
 1241 ... Clerbaux, C. (2021). Trends in spectrally resolved outgoing longwave
 1242 radiation from 10 years of satellite measurements. *npj Clim Atmos Sci*, 4,
 1243 48,<https://doi.org/10.1038/s41612-021-00205-7>.
- 1244 Wu, W., Liu, X., Lei, X., L. amd Xiong, Yang, Q., Yue, Q., Zhou, D., & Larar, A.
 1245 (2023). Single field-of-view sounder atmospheric product retrieval algorithm
 1246 : establishing radiometric consistency for hyper-spectral sounder retrievals.
 1247 *AMT*, 16, 4807-4832, <https://doi.org/10.5194/amt-16-4807-2023>.
- 1248 Zhou, D., Larar, A., Liu, X., Smith, W., Strow, L., Yang, P., ... Calbet, X. (2011).
 1249 Global Land Surface Emissivity Retrieved From Satellite Ultraspectral IR
 1250 Measurements. *IEEE Trans. Geosci. Remote Sens.*, 49(4), 1277-1290.